Journal of Computational Physics 501 (2024) 112766

Contents lists available at ScienceDirect

Journal of Computational Physics

journal homepage: www.elsevier.com/locate/jcp

# A novel vertex-centered finite volume method for solving Richards' equation and its adaptation to local mesh refinement

Yingzhi Qian [a,d], Xiaoping Zhang [b,*], Yan Zhu [a,*], Lili Ju [c], Alberto Guadagnini [d], Jiesheng Huang [a]

[a] State Key Laboratory of Water Resources and Hydropower Engineering Science, Wuhan University, Wuhan, 430072, Hubei, China
[b] School of Mathematics and Statistics, Wuhan University, Wuhan, 430072, Hubei, China
[c] Department of Mathematics, University of South Carolina, Columbia, 29208, SC, USA
[d] Dipartimento di Ingegneria Civile e Ambientale, Politecnico di Milano, Milano, Italy

ARTICLE INFO

*Keywords:*
Richards' equation
Vertex-centered finite volume method
Soil water movement
Nonmatching grids
Locally refined meshes

ABSTRACT

Accurate and efficient numerical simulations of soil water movement, as described by the highly nonlinear Richards' equation, often require local refinement near recharge or sink/source terms. In this paper, we present a novel numerical scheme for solving Richards' equation. Our approach is based on the vertex-centered finite volume method (VCFVM) and can be easily adapted to locally refined meshes. The proposed scheme offers some key features, including the definition of all unknowns over vertices of the primary mesh, expression of flux crossing dual edges as combinations of hydraulic heads at the vertices of the primary cell, and the capability to handle nonmatching meshes in the presence of local mesh refinement. For performance evaluation, soil water content and soil water potential simulated by the proposed scheme are benchmarked against results produced from HYDRUS (a widely used soil water numerical model) and the observed values in four test cases, including a convergence test case, a synthetic case, a laboratory experiment case and a field experiment case. The comparison results demonstrate the effectiveness and applicability of our scheme across a wide range of soil parameters and boundary conditions.

## 1. Introduction

Soil-water numerical models are effective tools to simulate the soil water content under natural or anthropogenic-induced scenarios, including, e.g., agricultural practices and crop growth. They have been broadly used to provide informed support to agricultural water management practices [16,21,7]. Existing soil-water numerical models mainly can be grouped into two categories according to their underlying governing equations. The first one is based on simplified or empirical expressions, whose core idea rests on mass balance, including SALTMOD [26], SWAT [1], and UBMOD [20], while the second one is based on physically-based kinetic equations, such as Richards' equation [31] describing the unsaturated soil water flow, including but not limited to SWAP [13] and HYDRUS [35]. Models based on empirical equations are widely used in large scale scenarios [30], such as basin and global scales,

* Corresponding authors.
*E-mail addresses:* xpzhang.math@whu.edu.cn (X. Zhang), zyan0701@163.com (Y. Zhu).

https://doi.org/10.1016/j.jcp.2024.112766
Received 30 August 2023; Received in revised form 5 January 2024; Accepted 8 January 2024

Available online 14 January 2024

due to their less requirements for input parameters and high computational efficiency. However, most of these models are usually limited to one-dimension or quasi two-dimension, and their accuracies are lower than those based on the Richards' equation [44].

Obtaining efficient and accurate numerical solutions of Richards' equation is still a key challenge [6] due to its high nonlinearity. Currently available computational softwares are characterized by strict requirements on grid size, especially within regions near recharge or sink/source terms. These include, e.g., locations near the soil surface in the presence of high evapotranspiration or recharge fluxes, or in the proximity of drippers, where fine grids are needed to suppress numerical errors [33]. Such high level of grid refinement might not be required at other locations in the system, but transitioning from a fine to coarse grid could still need a large number of nodes/elements. This issue can severely affect computational cost, especially under scenarios where multiple local refinements are needed. Existing conventional numerical strategies to solve Richards' equation are based on either finite difference, finite volume, or finite element schemes [6]. It is noted that finite volume [27] or finite element [35] approaches are typically implemented by discretizing most of the simulation domains through triangular or hexagonal elements. Local refinement could then be designed by adjusting the size of the elements. The number of elements adjacent to a given one is then equal to the number of its edges, which is a constrain that limits local refinement efficiency for traditional grids.

Resorting to nonmatching grids, which refers to those meshes whose elements could connect to more than one neighbor elements on certain edges, is appealing to increase efficiency of local refinement techniques for Richards' equation. Some approaches treat the fine and the coarse grids as different models, termed as child and parents models, respectively. These are either one-way [32] or iteratively coupled [22]. Starting from these schemes, considerable efforts have been devoted in development of numerical algorithms customized to solve elliptic and parabolic problems with nonmatching grids. The mixed finite element methods (MFEM) [10] have shown some benefits in dealing with nonmatching grid as compared against traditional finite element methods (FEM) (see [11,25, 42,8]), and possess good property in local mass-conservation. Nonmatching grids are also adopted in Discontinuous Galerkin (DG) finite element methods, and widely used in the area of multi-scale problems [17,4,12]. Besides the methods mentioned above, other multiscale models with ability to cope with nonmatching grids were also developed based on different spatial discretization methods, such as FDM [14], FVM [19], and mixed FVM [42]. Although substantial efforts have been made in developing algorithms with the ability to cope with nonmatching grids, there are still some key issues that need to be resolved [24]. For example, algorithms based on MFEMs are characterized by an auxiliary variable that cannot be eliminated from the system, thus requiring additional computational efforts. Finite element algorithms based on DG approach require additional consideration of multiple-valued boundary conditions at the nonmatching interface to ensure local conservation properties and appropriate enforcing of boundary conditions. Additionally, while some studies consider nonmatching grids in the context of fully saturated groundwater flow [42,14], the performance of these methods, in the presence of highly nonlinear dynamical systems described through the Richards' Equation, is still not fully appraised. Developing accurate and cost-efficient algorithms to solve the Richards' Equation via nonmatching grid discretization would critically enhance our ability to describe hydrological scenarios with high spatial resolution [44].

In this paper, a distinctive objective of our study is the design and development of a novel numerical scheme for the solution of the Richards' Equation across a two-dimensional horizontal and vertical system with arbitrary polygonal grids, including nonmatching grids. Our approach is based on a Vertex-Centered Finite Volume Method (hereinafter referred to as VCFVM) and sets all unknowns on grid vertices. It should be noted that the vertex-centered finite volume method has been widely studied for solving anisotropic diffusion/parabolic equations on general polygonal/polyhedral meshes in the past decade, see [41,40,45,36,5,29]. The numerical scheme proposed in this paper is partially inherited from [29], but substantial modifications in the spatial and temporal discretization have been made to consider the properties of Richards' equation, including the advection flux involved and the high nonlinearity between the soil hydraulic parameters and the soil water potential. Three types of quantities are involved in the scheme, corresponding to vertex, edge-midpoint, and cell-centered quantities. Edge-midpoint and cell-centered quantities, treated as the auxiliary ones, are eliminated by interpolation using vertex quantities, which is treated as the primary quantities. The flux crossing a lateral surface of the control volume centered around a mesh vertex is expressed as a function of the soil water potentials at the vertices of the grid element containing the lateral surface. A given row of the stiffness matrix of the system includes the entries stemming from formulating mass conservation for the control volume associated with the corresponding grid node. Since a control volume can be defined for each vertex, our scheme readily embeds treatment of nonmatching grids in the presence of local grid refinement. Four showcase scenarios are considered to numerically demonstrate the performance of our method, including a convergence test case, a synthetic case, a laboratory experiment case and a field experiment case. The performance of our VCFVM is also compared against HYDRUS [34], a widely used and tested numerical model.

The paper is organized as follows. The problem setting with Richards' equation is first introduced in Section 1.1. The spatial discretization based on VCFVM and the temporal discretization based Newton's method are then proposed in Sections 2 and 3, respectively. The details of the four test cases and corresponding numerical comparison results are presented in Section 4. Some conclusions are given in Section 5.

### 1.1. Richards' equation for soil water movement

Variably saturated soil water flow across a vertical two-dimensional spatial domain $\Omega \subset \mathbb{R}^2$ can be described by the Richards' equation as follows:

$$\nabla \cdot (\boldsymbol{K}(h)\nabla(h+z)) = \frac{\partial \theta(h)}{\partial t} + f(\boldsymbol{x},t), \quad (\boldsymbol{x},t) \in \Omega^T, \tag{1a}$$

$$h(\boldsymbol{x},t) = g_0(\boldsymbol{x}), \quad (\boldsymbol{x},t) \in \Omega^0, \tag{1b}$$

$$h(\boldsymbol{x},t) = g_1(\boldsymbol{x},t), \quad (\boldsymbol{x},t) \in \Gamma_D^T, \tag{1c}$$

$$\boldsymbol{K}(h)\nabla(h+z)\cdot\boldsymbol{n}(\boldsymbol{x}) = g_2(\boldsymbol{x}), \quad (\boldsymbol{x},t) \in \Gamma_N^T, \tag{1d}$$

where $\Omega^T = \Omega \times (0,T]$ is the spatial-temporal simulation domain of the problem, $\Omega^0 = \Omega \times \{0\}$ corresponds to the initial conditions, $\Gamma_D^T = \Gamma_D \times (0,T]$ and $\Gamma_N^T = \Gamma_N \times (0,T]$ denotes Dirichlet and Neumann boundary, respectively, $\boldsymbol{x} = (x,z)$ and $t$ are spatial position and time-stamp, respectively, the unknowns $h$ denotes the soil water potential ($[L]$) and $\theta(h)$ denotes the soil volumetric water content ($[-]$), $\nabla$ is the spatial gradient operator (e.g., $\nabla = (\partial/\partial x, \partial/\partial z)^T$), $g_0, g_1$ and $g_2$ are the specified initial, Dirichlet boundary, and Neumann boundary values, respectively, $\boldsymbol{n}(x)$ denotes the unit normal (outward) vector to $\Omega$ over the Neumann boundary, $f$ is the source/sink term ($[L^2T^{-1}]$), and $\boldsymbol{K}(h)$ is the soil hydraulic conductivity tensor taking the form of

$$\boldsymbol{K}(h) = \begin{pmatrix} K_{xx}(h) & K_{xz}(h) \\ K_{zx}(h) & K_{zz}(h) \end{pmatrix} \tag{2}$$

where $K_{xx}(h), K_{xz}(h), K_{zx}(h)$ and $K_{zz}(h)$ are the soil hydraulic conductivities in each direction ($[LT^{-1}]$), respectively. Note that the soil water capacity $C_w(h)$ ($[L^{-1}]$) is expressed as $C_w(h) = d\theta/dh$.

Closure of Eq. (1) requires constitutive relations to express $\theta(h)$ and $K(h)$. Here, we consider the widely used van Genuchten model [9], i.e.,

$$\theta(h) = \begin{cases} \theta_r + \dfrac{\theta_s - \theta_r}{(1+|\alpha h|^n)^m}, & h < 0, \\ \theta_s, & h \geq 0, \end{cases} \tag{3}$$

where $\theta_r$ and $\theta_s$ are the residual and saturated soil volumetric water contents ($[-]$), respectively, $\alpha$ is a parameter related to the mean pore-size ($[L^{-1}]$), $n$ is a parameter related to the pore-size distribution ($[-]$), and $m = 1 - 1/n$. The quantitative relation between $K(h)$ and $\theta(h)$ is formulated as:

$$K(h) = K_s S_e^{0.5}\left[1 - \left(1 - S_e^{\frac{1}{m}}\right)\right]^2, \tag{4}$$

where $K_s$ denotes saturated hydraulic conductivity ($[L/T]$) and $S_e$ is the effective saturation ($[-]$) defined by

$$S_e = \frac{\theta(h) - \theta_r}{\theta_s - \theta_r}. \tag{5}$$

**Remark 1.** In some scenarios, one may consider variably saturated soil water flow across a horizontal two-dimensional spatial domain. Under such situation, instead of (1a), the Richards' equation is expressed as

$$\nabla\cdot(\boldsymbol{K}(h)\nabla(h)) = \frac{\partial\theta(h)}{\partial t} + f(\boldsymbol{x},t), \quad (\boldsymbol{x},t) \in \Omega^T. \tag{6}$$

## 2. Spatial discretization of Richards' equation with VCFVM

### 2.1. Primary and dual meshes and placement of unknowns

For spatial discretization, the domain $\Omega$ is partitioned into nonoverlapping arbitrary polygonal cells, which constitute the primary mesh $\mathcal{M}$ and are identified through solid line segments in Fig. 1(a). Each primary cell is further partitioned into quadrilateral sub-cells by connecting the distinguished point (set as the geometric center of the primary cell here) with the midpoint of the cell edges (see dashed segments in Fig. 1(a)). The sub-cells sharing the vertex $\boldsymbol{x}_v$ in the primary mesh form a polygonal cell (shaded area denoted as $C_v^*$ in Fig. 1(a)), which is called the control volume (i.e. dual cell) associated with the vertex $\boldsymbol{x}_v$, and all these control volumes constitute the dual mesh of the domain $\Omega$. The set of all vertices except those on the Dirichlet boundary $\Gamma_D$ is denoted as $\mathcal{V}$. In addition, four sets are introduced, namely, the set of primary edges (resp. the primary cells) sharing the vertex $\boldsymbol{x}_v$, denoting as $\mathcal{E}_v$ (resp. $\mathcal{M}_v$), and the set of edges (resp. vertices) in the primary cell $C$, denoting as $\mathcal{E}_C$ (resp. $\mathcal{V}_C$).

Two types of unknowns are introduced, hereafter termed as the primary and auxiliary unknowns. The former is defined at the vertices of the primary mesh inside $\Omega$ and on the Neumann boundary $\Gamma_N$ (see solid circle in Fig. 1). The auxiliary unknowns, which will be eliminated later by using appropriate interpolations, are defined at the cell centers and edge midpoints of the primary mesh, denoted by circled dot and hollow circle in Fig. 1, respectively.

### 2.2. Numerical diffusive flux

In this subsection, we consider how to discretize the diffusive flux $\boldsymbol{K}(h)\nabla h$ in Eq. (1). Let $\boldsymbol{x}_v$ and $\boldsymbol{x}_{v'}$ be two interior vertices sharing an edge $\sigma$ in the primary cell $C$ (see Fig. 1(b)). Let $\boldsymbol{x}_\sigma$ and $\boldsymbol{x}_C$ be the midpoint of the edge $\sigma$ and the center of $C$, respectively, and $\boldsymbol{K}_C$ denote the constant restriction of $\boldsymbol{K}(h)$ on $C$, where the soil water potential $h$ on $C$ is approximated by

$$h_C = \frac{1}{n_C}\sum_{v\in\mathcal{V}_C} h_v, \tag{7}$$

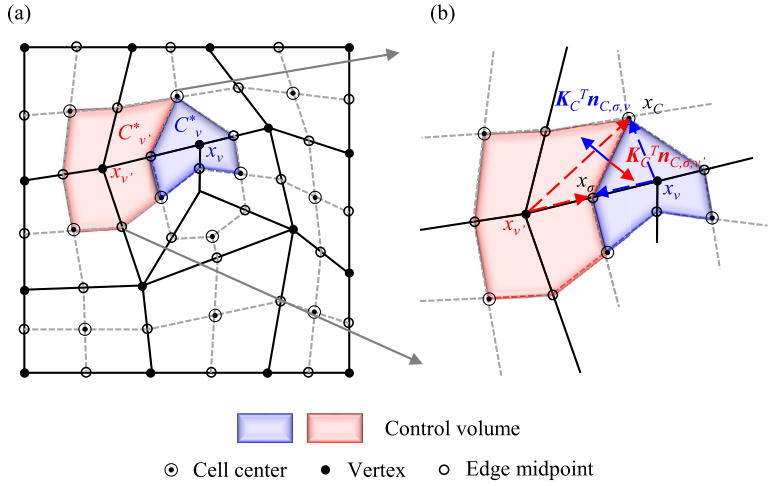


**Fig. 1.** Sketch maps of (a) the primary mesh (solid line) and the dual mesh (dashed line), (b) notations for the construction of the numerical flux. Note: $\boldsymbol{x}_v$ (and $\boldsymbol{x}_{v'}$), $\boldsymbol{x}_\sigma$ and $\boldsymbol{x}_C$ denote the specified vertex, the midpoint of the primary edge $\sigma$ and the center of the primary cell $C$, respectively; $K_C$ is the constant restriction of the hydraulic conductivity $K(h)$ on the primary cell $C$; $\boldsymbol{n}_{C,\sigma,v}$ refers to the unit vector (outwards) normal to the edge $\boldsymbol{x}_\sigma\boldsymbol{x}_C$ of the control volume associated with the vertex $\boldsymbol{x}_v$.

with $\mathcal{V}_C$ (resp. $n_C$) denoting the set (resp. number) of vertices in the cell $C$. In Fig. 1(b), $\boldsymbol{n}_{C,\sigma,v}$ (or $\boldsymbol{n}_{C,\sigma,v'}$) denotes the unit (outward) vector normal to the dual edge $\boldsymbol{x}_\sigma\boldsymbol{x}_C$. Clearly, $\boldsymbol{n}_{C,\sigma,v} = -\boldsymbol{n}_{C,\sigma,v'}$.

According to Darcy's law, the diffusive flux rate $\boldsymbol{v}$ at a given point within the cell $C$ can be defined by

$$\boldsymbol{v} = -\boldsymbol{K}_C \nabla h, \tag{8}$$

and the outflow of the control volume crossing the dual edge $\boldsymbol{x}_\sigma\boldsymbol{x}_C$ (Fig. 1 (b)) can be expressed as

$$F^d_{C,\sigma,v} = |\boldsymbol{x}_\sigma\boldsymbol{x}_C|\boldsymbol{v}\cdot\boldsymbol{n}_{C,\sigma,v} = -\nabla h\cdot\left(|\boldsymbol{x}_\sigma\boldsymbol{x}_C|\boldsymbol{K}_C^T\boldsymbol{n}_{C,\sigma,v}\right), \tag{9}$$

where $|\boldsymbol{x}_\sigma\boldsymbol{x}_C|$ denotes the length of $\boldsymbol{x}_\sigma\boldsymbol{x}_C$. The vector $|\boldsymbol{x}_\sigma\boldsymbol{x}_C|\boldsymbol{K}_C^T\boldsymbol{n}_{C,\sigma,v}$ can be decomposed as a linear combination of two vectors $\boldsymbol{x}_v\boldsymbol{x}_C$ and $\boldsymbol{x}_v\boldsymbol{x}_\sigma$:

$$|\boldsymbol{x}_\sigma\boldsymbol{x}_C|\boldsymbol{K}_C^T\boldsymbol{n}_{C,\sigma,v} = \alpha_{C,\sigma,v}(\boldsymbol{x}_C - \boldsymbol{x}_v) + \beta_{C,\sigma,v}(\boldsymbol{x}_\sigma - \boldsymbol{x}_v), \tag{10}$$

where

$$\begin{aligned}\alpha_{C,\sigma,v} &= \frac{|\boldsymbol{x}_\sigma\boldsymbol{x}_C|\boldsymbol{n}_{C,\sigma,v}^T\boldsymbol{K}_C^T\boldsymbol{R}(\boldsymbol{x}_\sigma - \boldsymbol{x}_v)}{(\boldsymbol{x}_C - \boldsymbol{x}_v)^T\boldsymbol{R}(\boldsymbol{x}_\sigma - \boldsymbol{x}_v)},\\ \beta_{C,\sigma,v} &= \frac{|\boldsymbol{x}_\sigma\boldsymbol{x}_C|\boldsymbol{n}_{C,\sigma,v}^T\boldsymbol{K}_C^T\boldsymbol{R}(\boldsymbol{x}_C - \boldsymbol{x}_v)}{(\boldsymbol{x}_\sigma - \boldsymbol{x}_v)^T\boldsymbol{R}(\boldsymbol{x}_C - \boldsymbol{x}_v)},\end{aligned} \tag{11}$$

and $\boldsymbol{R}$ is a rotation matrix that makes a vector rotate 90 degrees counterclockwise, i.e.,

$$\boldsymbol{R} = \begin{pmatrix} 0 & -1 \\ 1 & 0 \end{pmatrix}.$$

Substituting Eq. (10) into Eq. (9) leads to numerical diffusive flux

$$F^d_{C,\sigma,v} \simeq \alpha_{C,\sigma,v}(h_v - h_C) + \beta_{C,\sigma,v}(h_v - h_\sigma), \tag{12}$$

where $h_v$, $h_C$ and $h_\sigma$ denote the soil water potential $h$ at $\boldsymbol{x}_v$, $\boldsymbol{x}_C$ and $\boldsymbol{x}_\sigma$, respectively, and hereafter the symbol $\simeq$ indicates that the formula holds in the linearity-preserving sense, i.e., its truncation error vanishes if the solution is piecewise linear and the diffusion tensor is piecewise constant with respect to the primary mesh. Similarly, we can derive the numerical diffusive flux on the dual edge $\boldsymbol{x}_C\boldsymbol{x}_\sigma$ associated with the vertex $\boldsymbol{x}_{v'}$ as

$$F^d_{C,\sigma,v'} \simeq \alpha_{C,\sigma,v'}(h_{v'} - h_C) + \beta_{C,\sigma,v'}(h_{v'} - h_\sigma), \tag{13}$$

where

$$\alpha_{C,\sigma,\upsilon'} = \frac{|\boldsymbol{x}_\sigma \boldsymbol{x}_C| \boldsymbol{n}_{C,\sigma,\upsilon'}^T \boldsymbol{K}_C^T \boldsymbol{R}(\boldsymbol{x}_\sigma - \boldsymbol{x}_{\upsilon'})}{(\boldsymbol{x}_C - \boldsymbol{x}_{\upsilon'})^T \boldsymbol{R}(\boldsymbol{x}_\sigma - \boldsymbol{x}_{\upsilon'})},$$
$$\beta_{C,\sigma,\upsilon'} = \frac{|\boldsymbol{x}_\sigma \boldsymbol{x}_C| \boldsymbol{n}_{C,\sigma,\upsilon'}^T \boldsymbol{K}_C^T \boldsymbol{R}(\boldsymbol{x}_C - \boldsymbol{x}_{\upsilon'})}{(\boldsymbol{x}_\sigma - \boldsymbol{x}_{\upsilon'})^T \boldsymbol{R}(\boldsymbol{x}_C - \boldsymbol{x}_{\upsilon'})}. \tag{14}$$

Up till now, the auxiliary unknowns (for example, $h_\sigma$ and $h_C$) still exist in the numerical diffusive flux equations (12) and (13). In order to obtain a vertex-centered FV scheme, these auxiliary unknowns must be interpolated by primary unknowns. A desirable interpolation algorithm is usually required to be second-order, simple, topology-independent, discontinuity-independent and so on. As for the proposed scheme, since the auxiliary unknowns are defined at the centers and edge midpoints of the primary cells, they can be easily interpolated by the vertex unknowns. Let $\boldsymbol{x}_\sigma$ be the midpoint of $\sigma$ whose endpoints are $\boldsymbol{x}_\upsilon$ and $\boldsymbol{x}_{\upsilon'}$, then for the auxiliary unknowns defined at $\boldsymbol{x}_\sigma$, we have

$$h_\sigma = (h_\upsilon + h_{\upsilon'})/2. \tag{15}$$

Obviously, this simple interpolation algorithm satisfies all the aforementioned good proprieties. Substituting (7) and (15) into (9) and (13), we obtain the final numerical diffusive fluxes, still denoted by $F_{C,\sigma,\upsilon}^d$ and $F_{C,\sigma,\upsilon'}^d$, as below:

$$F_{C,\sigma,\upsilon}^d = \alpha_{C,\sigma,\upsilon}\left(h_\upsilon - \frac{1}{n_C}\sum_{\boldsymbol{x}_\upsilon \in \mathcal{V}_C} h_\upsilon\right) + \beta_{C,\sigma,\upsilon}\left(\frac{h_\upsilon - h_{\upsilon'}}{2}\right),$$
$$F_{C,\sigma,\upsilon'}^d = \alpha_{C,\sigma,\upsilon'}\left(h_{\upsilon'} - \frac{1}{n_C}\sum_{\boldsymbol{x}_\upsilon \in \mathcal{V}_C} h_\upsilon\right) + \beta_{C,\sigma,\upsilon'}\left(\frac{h_{\upsilon'} - h_\upsilon}{2}\right). \tag{16}$$

The following theorem exhibits the local conservation of the final numerical diffusive fluxes, which is crucial for the construction of our VCFVM scheme for Eq. (1).

**Theorem 1** *([29]). If the primary cell $C$ is a star-shaped one whose center is $\boldsymbol{x}_C$, then the two numerical diffusive fluxes in* (16) *satisfy*

$$F_{C,\sigma,\upsilon}^d + F_{C,\sigma,\upsilon'}^d = 0. \tag{17}$$

### 2.3. Numerical advection flux

For a vertical profile, the outflow of the control volume crossing the $\boldsymbol{x}_\sigma \boldsymbol{x}_C$ driven by gravitational potential $\boldsymbol{K}(h)\nabla z$, denoted as $F_{C,\sigma,\upsilon}^a$, should be included into the total numerical flux. The advection flux $F_{C,\sigma,\upsilon}^a$ has the similar form with the diffusive flux $F_{C,\sigma,\upsilon}^d$ defined in Eq. (9). Replacing the term $\nabla h$ in Eq. (9) by $\nabla z$ leads to

$$F_{C,\sigma,\upsilon}^a = -|\boldsymbol{x}_\sigma \boldsymbol{x}_C| \boldsymbol{K}_C \nabla z \cdot \boldsymbol{n}_{C,\sigma,\upsilon}. \tag{18}$$

Since the term $\nabla z = (0,1)^T$ is a constant vector, and (18) can be simplified as

$$F_{C,\sigma,\upsilon}^a = -|\boldsymbol{x}_\sigma \boldsymbol{x}_C| \boldsymbol{K}_C^z \cdot \boldsymbol{n}_{C,\sigma,\upsilon}, \tag{19}$$

where $\boldsymbol{K}_C^z$ denotes the vector formed by the second column of the diffusive tensor $\boldsymbol{K}_C$. Similarly, the numerical advection flux $F_{C,\sigma,\upsilon'}^a$ across the dual edge $\boldsymbol{x}_C \boldsymbol{x}_\sigma$ associated with the vertex $\boldsymbol{x}_{\upsilon'}$ can be defined by

$$F_{C,\sigma,\upsilon}^a = -|\boldsymbol{x}_\sigma \boldsymbol{x}_C| \boldsymbol{K}_C^z \cdot \boldsymbol{n}_{C,\sigma,\upsilon'}, \tag{20}$$

Due to the fact that $\boldsymbol{n}_{C,\sigma,\upsilon} = -\boldsymbol{n}_{C,\sigma,\upsilon'}$, it is easy to find

$$F_{C,\sigma,\upsilon}^a + F_{C,\sigma,\upsilon'}^a = 0, \tag{21}$$

which says that the local conservation of numerical advection fluxes is assured.

### 2.4. Vertex-centered finite volume discretization

For any control volume $C_\upsilon^*$ associated with vertex $\boldsymbol{x}_\upsilon \in \mathcal{V}$, the total flow, including the flow driven by the water potential and the gravitational potential, is the sum of the outflows crossing the dual edges of $C_\upsilon^*$, which leads to discretization of the left-hand term of Eq. (1a) as

$$F_\upsilon = \sum_{C \in \mathcal{M}_\upsilon} \sum_{\sigma \in \mathcal{E}_C \cap \mathcal{E}_\upsilon} (F_{C,\sigma,\upsilon}^d + F_{C,\sigma,\upsilon}^a), \quad \forall \boldsymbol{x}_\upsilon \in \mathcal{V}. \tag{22}$$

On the other hand, the integral of the right-hand side of Eq. (1a) over the control volume $C_\upsilon^*$ can be approximated by

$$\int_{C_v^*} \frac{\partial \theta(h)}{\partial t}\, d\boldsymbol{x} + \int_{C_v^*} f\, d\boldsymbol{x} \approx |C_v^*| \frac{\partial \theta(h_v)}{\partial t} + |C_v^*| f(\boldsymbol{x}_v), \quad \forall v \in \mathcal{V}, \tag{23}$$

where $|C_v^*|$ denotes the area of the control volume $C_v^*$. Combination of (22) and (23) yields the discretization of (1a):

$$\sum_{C \in \mathcal{M}_v} \sum_{\sigma \in \mathcal{E}_C \cap \mathcal{E}_v} (F_{C,\sigma,v}^d + F_{C,\sigma,v}^a) = |C_v^*| \frac{\partial \theta(h_v)}{\partial t} + |C_v^*| f(\boldsymbol{x}_v), \quad \forall v \in \mathcal{V}. \tag{24}$$

The matrix form of Eq. (24) is

$$\boldsymbol{A}(\boldsymbol{h})\boldsymbol{h} = \Lambda \frac{\partial \boldsymbol{\theta}(\boldsymbol{h})}{\partial t} + \Lambda \boldsymbol{f}, \tag{25}$$

where $\boldsymbol{A}(\boldsymbol{h})$ is the coefficient matrix which is nonlinear in terms of $\boldsymbol{h}$, $\boldsymbol{\theta}(\boldsymbol{h})$ is a vector whose entries are $\{\theta(h_v) : \boldsymbol{x}_v \in \mathcal{V}\}$, $\Lambda$ is a diagonal matrix whose diagonal entries are $\{|C_v^*| : \boldsymbol{x}_v \in \mathcal{V}\}$, and $\boldsymbol{f}$ is a vector whose entries are $\{f(x_v) : \boldsymbol{x}_v \in \mathcal{V}\}$. The spatial accuracy of our VCFVM scheme (25) is expected to be of second-order in the optimal case. It is also worth noting that our VCFVM scheme is naturally applicable to various matching or nonmatching grids and local mesh refinement methods as discussed later in numerical experiments.

## 3. Temporal discretization and adaptive time stepping

In order to obtain a fully discrete FVM, it is now necessary to discretize the time derivative in eq. (25). Such a procedure which takes care of spatial discretization before temporal discretization is called the method of lines (MOL). It is commonly used in other studies for Richards' equation, see e.g. [23,6].

### 3.1. Backward Euler scheme and Newton-Raphson method

To implement MOL, we need to partition the time domain $[0, T]$ into

$$0 = t_0 < t_1 < \cdots < t_N = T,$$

with the time step size $\tau^{n+1} = t_{n+1} - t_n$ for $n = 0, 1, \cdots, N-1$. By adopting the linearization technique over the term $\boldsymbol{A}(\boldsymbol{h})$ in Eq. (25), we get the backward Euler scheme

$$\boldsymbol{A}(\boldsymbol{h}^n)\boldsymbol{h}^{n+1} = \Lambda \frac{\boldsymbol{\theta}(\boldsymbol{h}^{n+1}) - \boldsymbol{\theta}(\boldsymbol{h}^n)}{\tau^{n+1}} + \Lambda \boldsymbol{f}^{n+1}, \tag{26}$$

where $\boldsymbol{h}^n$ is an approximation of $\boldsymbol{h}(t_n)$. Although the backward Euler scheme (26) only has first-order accuracy, it is often used for temporal discretization of Richards' equation because it provides good stability properties and remains simple to work with adaptive time stepping.

The backward Euler scheme (26) is nonlinear in terms of solution of $\boldsymbol{h}^{(n+1)}$, thus it needs to be solved by using nonlinear system solvers, such as Picard's and Newton-Raphson methods. Many derivative methods, including modified Newton-Raphson, mixed Picard-Newton, quasi-Newton, L-scheme and so on, have been developed to solve eq. (26). Studies have been carried out to compare these methods for solving Richards' equation, see e.g. [28,15,18]. They emphasized that Picard's iteration and even Newton-Raphson scheme are very sensitive and cannot convergence systematically due to the formulation of Richards' equation, initial and boundary condition and the nonlinearities of constitutive laws.

As reported in [34], as the Newton-Raphson method has been shown to provide excellent results in terms of minimizing the mass balance error [3], it has been used as a temporal discretization strategy in HYDRUS. For this reason, we adopt the Newton-Raphson method for solving (26). Of course, the aforementioned temporal discretization methods can be also used without any technical issue. Specifically, the Newton-Raphson method for solving (26) at each time step $n$ is given by: set $\boldsymbol{h}_0^{n+1} = \boldsymbol{h}^n$, then for $k = 0, 1, \cdots$, solve the linear system

$$\boldsymbol{A}(\boldsymbol{h}^n)\boldsymbol{h}_{k+1}^{n+1} = \Lambda \boldsymbol{C}_w(\boldsymbol{h}_k^{n+1}) \frac{\boldsymbol{h}_{k+1}^{n+1} - \boldsymbol{h}_k^{n+1}}{\tau^{n+1}} + \Lambda \frac{\boldsymbol{\theta}(\boldsymbol{h}_k^{n+1}) - \boldsymbol{\theta}(\boldsymbol{h}^n)}{\tau^{n+1}} + \Lambda \boldsymbol{f}^{n+1}, \tag{27}$$

where $\boldsymbol{C}_w(\boldsymbol{h}_k^{n+1})$ is a diagonal matrix whose diagonal entries are $\{C_w(h_{v,k}^{n+1}) : \boldsymbol{x}_v \in \mathcal{V}\}$, and the subscript $k$ denotes the $k$-th iteration at current time level. One important choice for nonlinear iterative process is the stopping criterion which is set for this study as

$$\frac{\|\boldsymbol{h}_{k+1}^{n+1} - \boldsymbol{h}_k^{n+1}\|}{\|\boldsymbol{h}_k^{n+1}\|} < \epsilon, \tag{28}$$

where $\epsilon$ is a user-defined tolerance.

### 3.2. Adaptive time stepping

Time adaption is driven by the convergence of the nonlinear solver. On the one hand, transient simulation is difficult to converge if the time step is too large, but on the other hand, shorter time steps means more time steps, and result in significant computational overhead. This is the reason why time adaptation is very attractive and common for solving the Richards' equation. Different strategies can be used to adjust the time step size [6], which can be either heuristic and mainly depend on convergence performance of the nonlinear solver, or rational and based on error control. The latter ones are usually more efficient, but heuristic methods are still widely adopted due to their simplicity.

For this study, we use a classic approach, which is to increase or decrease the time step size according to the previous number of iterations $N_{\text{it}}$ from the nonlinear solver such as [3,28]. Specifically, the time step size will be updated as follows:

$$\tau^{n+1} = \lambda \tau^n, \quad \lambda = \begin{cases} 0.7, & N_{\text{it}} > 7, \\ 1, & 3 \le N_{\text{it}} \le 7, \\ 1.3, & N_{\text{it}} < 7. \end{cases} \tag{29}$$

With this strategy, the nonlinear solver is more robust because the time step is adjusted until success of convergence independently on the initial time step $\tau^0$. Noted that for numerical stability, small time step size could be required, especially for the soil with high nonlinear soil water characteristic curve and those scenarios soil rapidly change from dry to wet. Up till now, we obtain the fully discrete numerical scheme of the VCFVM, which is given in Algorithm 1 for clarity.

**Algorithm 1:** Vertex-centered finite volume methods for solving Richards' equation.

**Input:** The parameters $\theta_s, \theta_r, \alpha, n$ in the van Genuchten model (3), the inital value $g_0$, the boundary values $g_1$ and $g_2$, the saturated hydraulic conductivity $K_s$, and the spatial mesh $\mathcal{M}$

```
Compute the initial soil water potential h of each vertex according to g_0;
Compute C_w(h) of each vertex according to C_w(h) = dθ/dh;
for n = 1, 2, ··· do
    Compute the soil water potential h of each cell according to Eq. (7);
    Compute the soil hydraulic conductivity K of each cell according to Eq. (4);
    Assemble the stiffness matrix A(h^n) and the source vector f^{n+1} in Eq. (27);
    Solve the linear system Eq. (27);
    if the convergence criterion (28) is satisfied then
        Exit
    Compute C_w(h) of each vertex according to C_w(h) = dθ/dh;
    Adjust next time step size according to Eq. (29);
```

## 4. Numerical experiments

Four test cases, including a convergence test case, a synthetic case, a laboratory experiment case and a field experiment case, are investigated to evaluate the accuracy and efficiency of VCFVM, and the corresponding results are compared with the benchmarks, i.e., the observed values, if existed, and/or results simulated by HYDRUS or VCFVM itself on a higher resolution mesh. The implementation of VCFVM is developed based on C++, and is run in Ubuntu 18.04 with GCC 7.3.0. We set the error tolerance $\epsilon = 10^{-6}$ in our experiments.

To quantify the simulation discrepancies between VCFVM and the benchmarks, two evaluation indices, including the mean absolute error (MAE) and the relative root mean square error (RRMSE), are considered, which are defined as follows,

$$\text{MAE} = \sum_{v \in \mathcal{V}} |u_v - u_v^*| |C_v^*|, \tag{30}$$

$$\text{RRMSE} = \sqrt{\frac{\sum_{v \in \mathcal{V}} (u_v - u_v^*)^2 |C_v^*|}{\sum_{v \in \mathcal{V}} u_v^{*2}}}, \tag{31}$$

where $u_v$ and $u_v^*$ are the simulated value produced by VCFVM and the value of benchmark at the vertex $v$, respectively, and $C_v^*$ is the control volume associated with the vertex $v$. Note that here $u$ could be either soil water potential $h$ or soil water content $\theta$. In this study, $\theta$ is used in the synthetic case and the field experiment case, and $h$ is used in the convergence case and laboratory experiment case. The MAE and the RRMSE values close to 0 indicate the accuracy of the algorithm. Moreover, we also define the convergence rate $R_\alpha$ as below,

$$R_\alpha = \frac{\log(\text{RRMSE}(s_1)/\text{RRMSE}(s_2))}{\log(s_1/s_2)}$$

where $s_1$ and $s_2$ are the spatial (or temporal) sizes of two successive spatial meshes (or temporal grids). In addition to the above evaluation indices, we also consider the total CPU time as another evaluation index to show the efficiency of VCFVM when dealing with nonmatching meshes. The details of each case setting as well as the results are illustrated below.

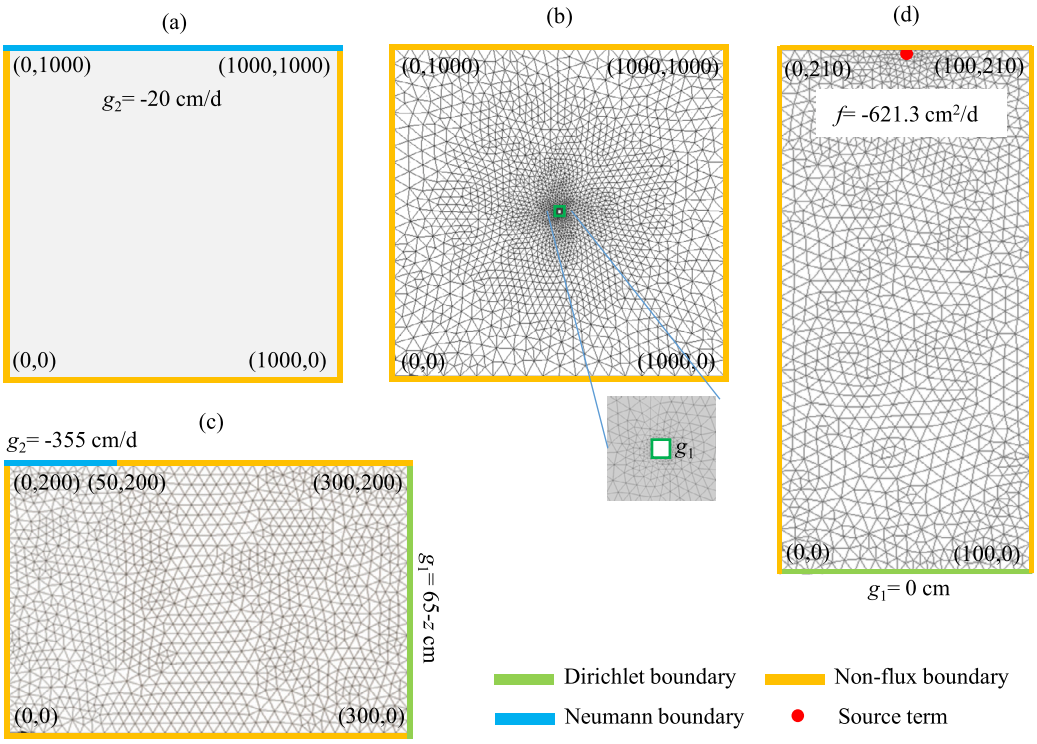


**Fig. 2.** Boundary conditions of (a) the convergence test case, and the boundary conditions and fine grids used in (b) the synthetic case, (c) the laboratory experiment case and (d) the field experiment case.

### *4.1. Convergence test case*

Here we employ a test case to investigate the spatial and temporal accuracy of the VCFVM. The simulation profile is a two-dimensional horizontal square area, with width 1000 cm, i.e., $\Omega = [0, 1000] \times [0, 1000]$ cm. Three of the external boundaries are set as homogeneous Neumann boundaries, while the last one is set as an inhomogeneous Neumann boundary with value $-20$ cm/d. The temporal domain is $T = [0, 20]$ d. The simulation domain is fulfilled with homogeneous and isotropic Loam soil (the hydraulic parameters are listed in Table 3), and the initial soil water content is set as 0.30 cm$^3$/cm$^3$. The settings of this case are shown in Fig. 2(a), and can be described as follows,

$$\theta(\boldsymbol{x}, t) = 0.30 \text{ cm}^3/\text{cm}^3, \quad (\boldsymbol{x}, t) \in \Omega^0,$$
$$\boldsymbol{K}(h)\nabla h \cdot \boldsymbol{n} = 0 \text{ cm/d}, \quad x = 0 \text{ or } 1000 \text{ cm, or } z = 0 \text{ cm},$$
$$\boldsymbol{K}(h)\nabla h \cdot \boldsymbol{n} = -20 \text{ cm/d}, \quad z = 1000 \text{ cm}.$$

*Spatial accuracy* To investigate the spatial accuracy of the VCFVM, we adopted the uniform square meshes, denoted as M1-a to M1-f, with different resolutions. In addition, nonmatching grid meshes, denoted as M1-g to M1-j, and distorted meshes (Kershaw mesh), denoted as M1-k to M1-n, are also adopted to investigate the spatial accuracy of the VCFVM with special meshes. The schematic diagrams of the three kinds of meshes mentioned above are shown in Fig. 3. In this case, the time step size is set as a sufficiently small constant value 0.05 d. Since there is no analytical solution for this problem, we use the approximate solution on the finest uniform square mesh M1-f as benchmark. The corresponding results, including the detailed information of the meshes, RRMSE, and convergence rates, are listed in Table 1, from which we see that the accuracy of the VCFVM using nonmatching grid meshes and Kershaw meshes are consistent to those using uniform square meshes, and the expected second-order accuracy of the VCFVM in space is achieved for all of the meshes.

*Temporal accuracy* To investigate the temporal accuracy of the VCFVM, we perform numerical tests on the spatial mesh M1-c, and temporal grids with different time step sizes, i.e. 0.5, 1, 1.5, 2.0, 4.0 d. We also take the approximated solution on M1-f as benchmark. Numerical results shown in Table 2 exhibit the first-order accuracy of our VCFVM in time.

*Stability analysis* Furthermore, we investigate the choice of the time step size on the stability of the proposed scheme, which is influenced by many factors, including the soil's highly nonlinear property, initial conditions and boundary conditions, as well as the Newton-Raphson's iteration in each time step and the error growth of the semi-implicit scheme (27). Due to these complexities, the

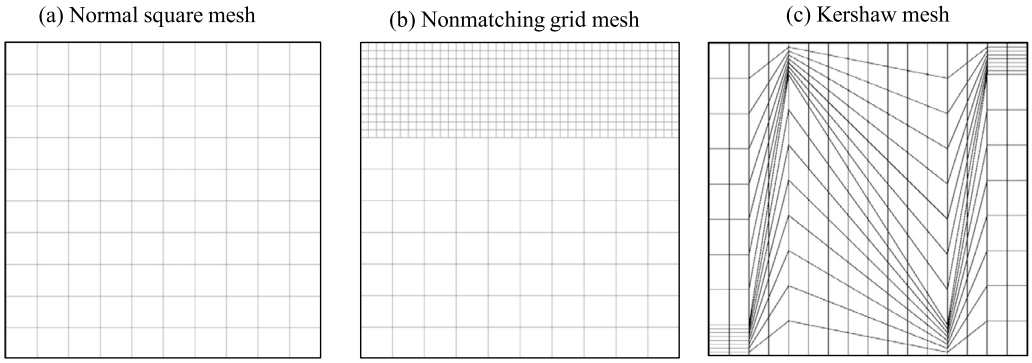


**Fig. 3.** Meshes used in the convergence test case.

**Table 1**
The meshes, RRMSE and convergence rates of our VCFVM in space using different meshes.

| Mesh type | Mesh id | Mesh size (cm) | RRMSE | Convergence rate |
|---|---|---|---|---|
| Square meshes | M1-a | 50.0 | 0.0137 | - |
| | M1-b | 40.0 | 0.0092 | 1.78 |
| | M1-c | 25.0 | 0.0040 | 1.77 |
| | M1-d | 20.0 | 0.0025 | 2.11 |
| | M1-e | 16.7 | 0.0017 | 1.96 |
| | M1-f | 12.5 | - | - |
| Nonmatching grids meshes | M1-g | 100.0 | 0.0581 | - |
| | M1-h | 50.0 | 0.0149 | 1.96 |
| | M1-i | 25.0 | 0.0041 | 1.86 |
| | M1-j | 12.5 | 0.0009 | 2.19 |
| Kershaw meshes | M1-k | 125.0 | 0.1163 | - |
| | M1-l | 62.5 | 0.0234 | 2.31 |
| | M1-m | 31.3 | 0.0060 | 1.84 |
| | M1-n | 15.6 | 0.0015 | 2.13 |

**Table 2**
The grids, RRMSE and convergence rates of our VCFVM in time.

| Temporal grid | G1-a | G1-b | G1-c | G1-d | G1-e |
|---|---|---|---|---|---|
| Grid size (d) | 4 | 2 | 1.5 | 1 | 0.5 |
| RRMSE | 0.0469 | 0.0265 | 0.0198 | 0.0136 | 0.0070 |
| Convergence rate | - | 0.82 | 1.02 | 0.92 | 0.95 |

stability analysis of the scheme is very hard to explore theoretically, thus we try to study it through some numerical experiments, where the soil in the simulation domain are set as loam and sand, the initial soil water potential is set as $-100$ cm, and the values of the Neumann boundary are set as $-1$ cm/d and $-5$ cm/d for loam and sand, respectively. The soil water characteristic curves (SWCC) are shown in Fig. 4, from which we can see that the nonlinearity of the SWCC for sand soil is significantly higher than loam. For comparison, we take the approximate solutions produced by the proposed scheme with very small time step sizes as the reference solutions, and set an observation point on the Neumann boundary. The relative errors along each timestamp at this point are evaluated to demonstrate the stability of the scheme for different time step sizes. It can be found in Fig. 5 that 1) these relative errors oscillate over time and tend to be stable with time go on; 2) although there are oscillations, the smaller the time step size, the smaller the errors on each timestamp; 3) for soils with moderate nonlinear SWCC (such as loam), even large time steps (such as $dt = 1.0$ d) can still ensure the convergence of the scheme, but it is still recommended to choose a relatively smaller time step to ensure that the errors on all timestamps are small; 4) for soils with highly nonlinear SWCC (such as sand), larger time step size could result in the divergence of the scheme, and an example of $dt = 0.04$ d for sand, denoted as the red circle in Fig. 5(b), shows that blow-up occurs at the first time step due to the failure of the Newton-Raphson iteration.

### *4.2. Synthetic case*

This case is a synthetic one, which is designed to evaluate the applicability of VCFVM to a wide range of soil hydraulic parameters. The simulation profile is a two-dimensional horizontal profile, whose spatial domain is set as $\Omega = [0, 1000] \times [0, 1000]$ cm, with a square opening with side length 10 cm in the center. All the external boundaries are set as no-flux boundaries and the edges of the

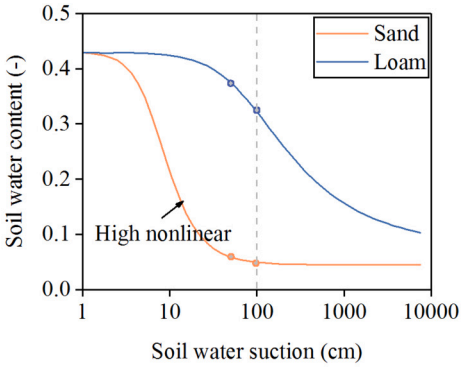


**Fig. 4.** The soil water characteristic curves of sand and loam soil.

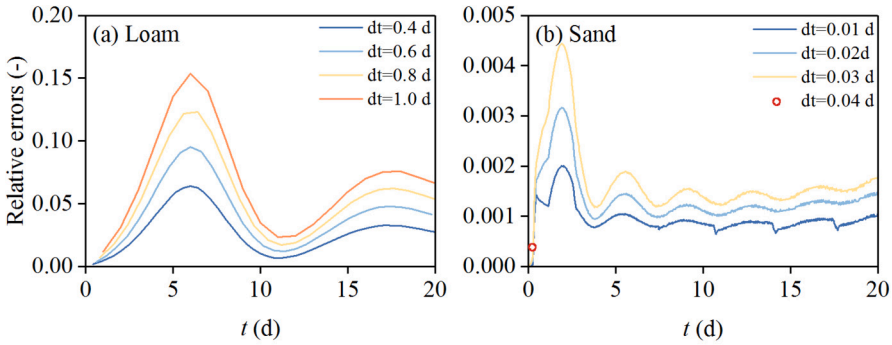


**Fig. 5.** The relative errors along the timestamps for different time step sizes under two scenarios. (For interpretation of the colors in the figure(s), the reader is referred to the web version of this article.)

**Table 3**
The soil hydraulic parameter values of van Genuchten model in the synthetic case.

| Soil types (cm) | $\theta_r(-)$ | $\theta_s(-)$ | $\alpha(\mathrm{cm}^{-1})$ | $n(-)$ | $K_s(\mathrm{cm/d})$ |
|---|---|---|---|---|---|
| Sand | 0.045 | 0.43 | 0.145 | 2.68 | 712.8 |
| Loamy sand | 0.057 | 0.41 | 0.124 | 2.28 | 350.2 |
| Sandy loam | 0.065 | 0.41 | 0.075 | 1.89 | 106.1 |
| Loam | 0.078 | 0.43 | 0.036 | 1.56 | 24.96 |
| Silt | 0.034 | 0.46 | 0.016 | 1.37 | 6 |
| Silt loam | 0.067 | 0.45 | 0.02 | 1.41 | 10.8 |
| Sandy clay loam | 0.1 | 0.39 | 0.059 | 1.48 | 31.44 |
| Clay loam | 0.095 | 0.41 | 0.019 | 1.31 | 6.24 |
| Silty clay loam | 0.089 | 0.43 | 0.01 | 1.23 | 1.68 |
| Sandy clay | 0.1 | 0.38 | 0.027 | 1.23 | 2.88 |
| Silty clay | 0.07 | 0.36 | 0.005 | 1.09 | 0.48 |
| Clay | 0.068 | 0.38 | 0.008 | 1.09 | 4.8 |

square opening are set as Dirichlet boundaries, with value of $g_1$ cm. The soil property is assumed to be homogeneous and isotropic. To demonstrate the robustness of VCFVM with wide range of soil hydraulic parameters, 12 kinds of soil in the published literature [2] are used in this case, and the parameters of each soil are given in Table 3. The temporal domain is $T = [0, T_E]$ d, and the initial time step is set as $10^{-2}$ d. The boundary conditions of this test case are shown in Fig. 2(b), and the initial and boundary conditions are described as follows,

$$\begin{aligned} \theta(\boldsymbol{x},t) &= \theta_0\ \mathrm{cm}^3/\mathrm{cm}^3, && (\boldsymbol{x},t)\in\Omega^0,\\ h(\boldsymbol{x},t) &= g_1\ \mathrm{cm}, && \boldsymbol{x}\in\Gamma_{in},\\ \boldsymbol{K}(h)\nabla h\cdot\boldsymbol{n} &= 0\ \mathrm{cm/d}, && \boldsymbol{x}\in\Gamma_{out}, \end{aligned}$$

where $\Gamma_{in} = [495\ \mathrm{cm}, 505\ \mathrm{cm}] \times \{495\ \mathrm{cm}, 505\ \mathrm{cm}\} \bigcup \{495\ \mathrm{cm}, 505\ \mathrm{cm}\} \times [495\ \mathrm{cm}, 505\ \mathrm{cm}]$ and $\Gamma_{out} = [0\ \mathrm{cm}, 1000\ \mathrm{cm}] \times \{0\ \mathrm{cm}, 1000\ \mathrm{cm}\} \bigcup \{0\ \mathrm{cm}, 1000\ \mathrm{cm}\} \times [0\ \mathrm{cm}, 1000\ \mathrm{cm}]$.

This case is simulated by VCFVM using a triangular mesh which is locally refined near the inner opening hole, shown in Fig. 2(b), and benchmarked against the results simulated by HYDRUS using the same mesh. It should be noted that locally refined mesh is

**Table 4**
The values of initial soil water content $\theta_0$, Dirichlet boundary $g_1$ and temporal domain $T_E$ of different soil types in the synthetic case.

| Soil type | $\theta_0$($cm^3/cm^3$) | $g_1$(cm) | $T_E$(d) |
|---|---|---|---|
| Sand, Loamy sand, Sandy loam | 0.1 | -10 | 20 |
| Loam, Silt, Silt loam, Sandy clay loam, Clay loam | 0.25 | 0 | 20 |
| Sandy clay | 0.3 | 0 | 100 |
| Silty clay loam | 0.3 | -100 | 100 |
| Silty clay | 0.3 | -100 | 500 |
| Clay | 0.3 | -10 | 500 |

**Table 5**
Basic information of the meshes used in the last three cases and the corresponding CPU time.

| Case | Mesh type | # of vertices | # of cells | CPU time (s) |
|---|---|---|---|---|
| Synthetic | Fine | 1934 | 3772 | / |
| Laboratory experiment | Fine | 1231 | 2350 | 4.27(VCFVM)/ 3.74(HYDRUS) |
| | M2-a | 72 | 51 | 0.95 |
| | M2-b | 160 | 117 | 1.36 |
| | M2-c | 362 | 276 | 2.01 |
| Field experiment | Fine | 1106 | 2095 | 2.13(VCFVM)/ 1.84 (HYDRUS) |
| | M3-a | 61 | 44 | 0.45 |
| | M3-b | 61 | 60 | 0.54 |
| | M3-c | 138 | 110 | 0.81 |
| | M3-d | 391 | 344 | 1.18 |

**Table 6**
The MAE and RRMSE of VCFVM compared to HYDRUS in the synthetic case.

| Soil types | Simulation domain | | Observation point | |
|---|---|---|---|---|
| | MAE | RRMSE(%) | MAE | RRMSE(%) |
| Sand | 0.0006 | 0.5 | 0.0017 | 1.2 |
| Loamy sand | 0.0009 | 0.7 | 0.0023 | 1.3 |
| Sandy loam | 0.0011 | 0.8 | 0.0042 | 1.9 |
| Loam | 0.0006 | 0.2 | 0.0017 | 0.4 |
| Silt | 0.0011 | 0.4 | 0.0092 | 2.6 |
| Silt loam | 0.0009 | 0.3 | 0.0060 | 1.6 |
| Sandy clay loam | 0.0005 | 0.2 | 0.0023 | 0.7 |
| Clay loam | 0.0009 | 0.3 | 0.0090 | 2.7 |
| Silty clay loam | 0.0002 | 0.1 | 0.0005 | 0.2 |
| Sandy clay | 0.0004 | 0.1 | 0.0036 | 1.1 |
| Silty clay | 0.0001 | 0.0 | 0.0005 | 0.2 |
| Clay | 0.0003 | 0.1 | 0.0034 | 1.0 |

necessary for this case due to not only the deformed boundary shape caused by the opening hole, but also the high hydraulic gradient near the inner boundary. The values of $g_1$, $T_E$ and $\theta_0$, given in Table 4, vary in different soil textures and the basic information of the mesh is provided in Table 5.

The absolute difference between the approximate soil water content ($\theta$) simulated by VCFVM and HYDRUS are shown in Fig. 6, from which we can see that this difference varies among different soil properties, and mainly appears near the wetting front, and becomes negligible in the remain area. Furthermore, the MAE and RRMSE of VCFVM in the whole domain (compared to HYDRUS) are listed in Table 6, and it can be found that the MAE ranges from 0.0001 to 0.0011, and the RRMSE ranges from 0.0% to 0.8%.

To understand the accuracy of VCFVM over time, we set an observation point at $O$(500.5 cm, 549.7 cm). The approximated soil water contents ($\theta$) at $O$ simulated by VCFVM and HYDRUS under different kinds of soil properties are shown in Fig. 7, from which we can see that both of them are almost completely matched. Since the observation point $O$ is close to the opening hole, the errors at $O$ are expected to represent the errors at the wetting front (according to Fig. 6). Quantitatively, as listed in Table 6, the MAE of VCFVM at $O$ (compared to HYDRUS) under different kinds of soil properties range from 0.0005 to 0.0092 $cm^3/cm^3$, and the corresponding RRMSE range from 0.2% to 2.6%. Although the errors are higher than those of the simulation domain, all of them are within an acceptable range, which demonstrate the accuracy and applicability of VCFVM to the wide range of soil types.

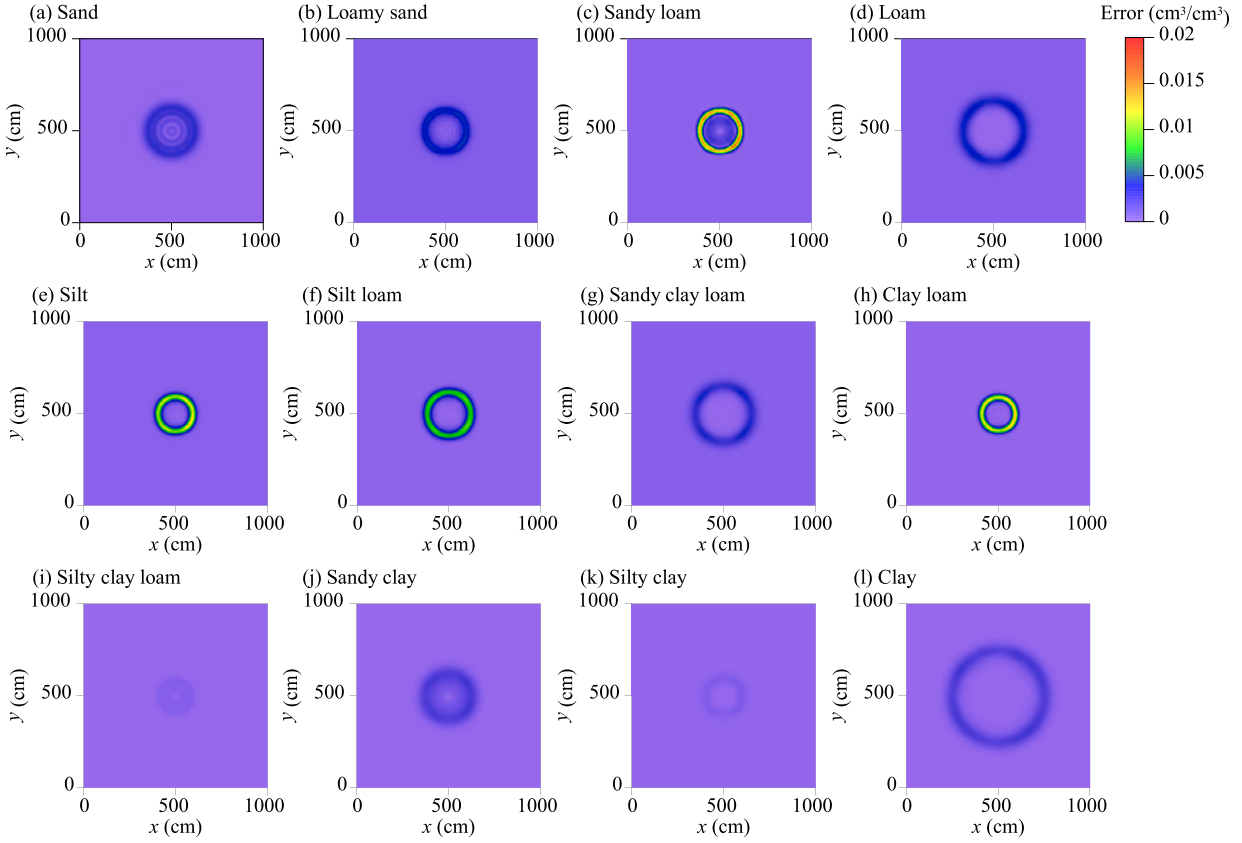


**Fig. 6.** Discrepancies between the simulated results of VCFVM and HYDRUS in the whole simulation domain in the synthetic case.

**Table 7**
The soil hydraulic parameter values of van Genuchten model in the laboratory experiment case.

| Soil depth (cm) | $\theta_r(-)$ | $\theta_s(-)$ | $\alpha(cm^{-1})$ | $n(-)$ | $K_s(cm \cdot d^{-1})$ |
|---|---|---|---|---|---|
| 0-200 | 0.01 | 0.30 | 0.033 | 4.1 | 840 |

### 4.3. *Laboratory experiment case: 2-D water table recharge experiment*

This case is a two-dimensional water table recharge laboratory experiment conducted by [39]. The groundwater levels at different positions and at different time stamps (0.08, 0.13, 0, 17 and 0.33 d) were observed during the experiment, and the data set was widely used in many previous researches to evaluate the performance of proposed algorithms [37,38,43]. The experimental setup consisted of a 600 by 200 cm tank containing sandy soil. The initial water table elevation was 65 cm from the bottom. A constant flux rate of $q = -355$ cm/d (the negative sign represents the flow towards the simulation domain) was applied across the center 100 cm of the soil surface while the rest of the surface was covered to prevent evaporation. Due to the symmetry of the experiment, only half of the experiment was modelled and the spatial domain was thus 300 by 200 cm, i.e., $\Omega = [0, 300] \times [0, 200]$ cm. The temporal domain is $T = [0, 0.333]$ d, and the initial time step is set as $10^{-4}$ d. The soil texture is assumed to be homogeneous and isotropic, the soil hydraulic parameters in the van Genuchten model are given in Table 7. The initial and boundary conditions of this case are shown in Fig. 2(c), which are described in detail as follows,

$$h(\boldsymbol{x}, 0) = 65 - z \text{ cm}, \ \boldsymbol{x} \in \Omega,$$

$$h(\boldsymbol{x}, t) = 65 - z \text{ cm}, \ x = 300 \text{ cm},$$

$$K(h)\nabla(h+z)\cdot \boldsymbol{n}(\boldsymbol{x}) = \begin{cases} -355 \text{ cm/d}, & 0 \le x \le 50 \text{ cm}, \ z = 200 \text{ cm}, \\ 0 \text{ cm/d}, & 50 \le x \le 300 \text{ cm}, \ z = 200 \text{ cm}, \\ 0 \text{ cm/d}, & x = 0 \text{ cm or } z = 0 \text{ cm}. \end{cases}$$

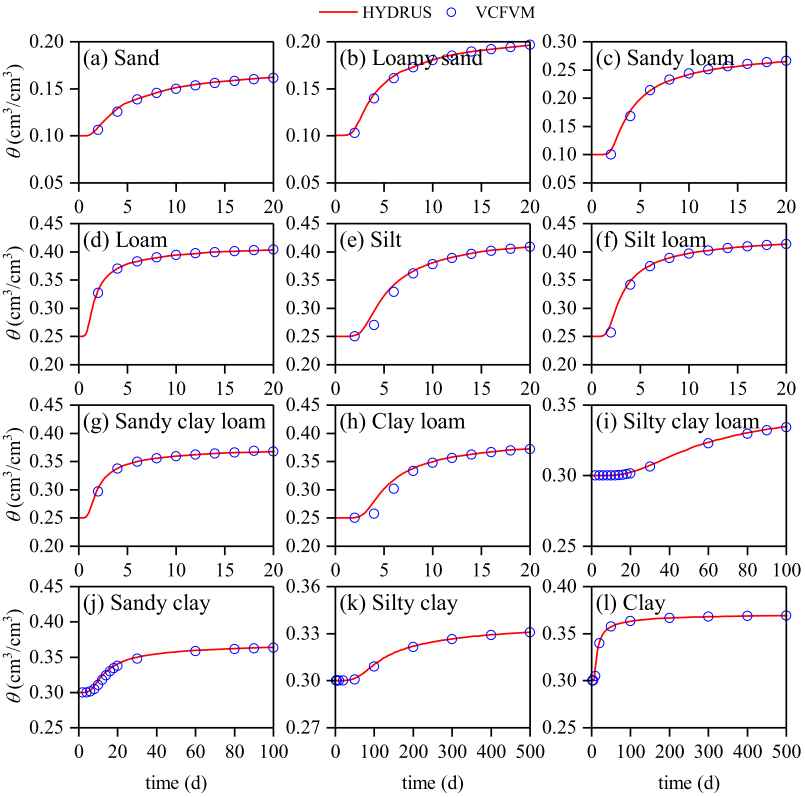


**Fig. 7.** The simulated soil water contents at the observation point obtained by VCFVM and HYDRUS with different soil types in the synthetic case.

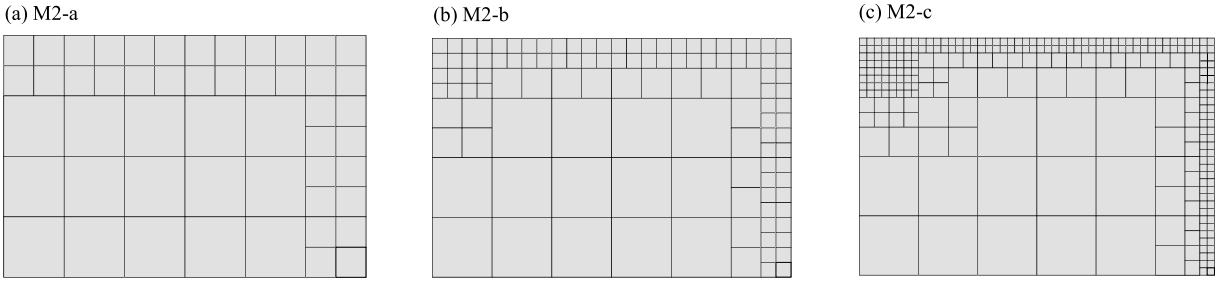


**Fig. 8.** Locally refined meshes used in the laboratory experiment case.

This case is first simulated by VCFVM using a fine mesh, as illustrated in Fig. 2(c), and the results are compared to the observed values provided by [39], and the results simulated by HYDRUS using the same mesh. To evaluate the accuracy and efficiency of VCFVM, this case is further simulated by VCFVM using different locally refined meshes. Since the flux rate is high near the recharge boundary and the Dirichlet boundary, these locations are selected for local refinement, and three nonmatching meshes are adopted for this end, which are denoted as M2-a, M2-b and M2-c and shown in Fig. 8. The basic information of the fine mesh and the three locally refined meshes used in this case are given in Table 5.

The soil water potentials ($h$) in the whole simulation domain at different timestamps simulated by VCFVM and HYDRUS using the same fine mesh, as well as the observed groundwater levels are shown in Fig. 9. The groundwater levels (see the contour line with value of 0 cm) simulated by both VCFVM and HYDRUS are close to the observed groundwater levels (see black circles), which demonstrate that both VCFVM and HYDRUS can be accurately applied to this case. Instead of using the observed values as benchmark, we choose the soil water potentials simulated by HYDRUS using a finer mesh as benchmark to quantify the accuracy of VCFVM in this case. The MAE of the soil water potential simulated by VCFVM are 0.267 cm, 0.379 cm, 0.383 cm, and 0.389 cm at 0.083 d, 0.125 d, 0.167 d and 0.333 d, respectively, and the corresponding RRMSE are 0.5%, 0.7%, 0.7% and 0.8%, which demonstrate the accuracy of VCFVM in the laboratory experiment case.

To show the superiority of VCFVM when using locally refined meshes, the soil water potentials in the whole domain at 0.333 d are simulated by VCFVM using the fine mesh, and the aforementioned locally refined meshes (M2-a, M2-b and M2-c), respectively. The corresponding results, including the contour lines, the heat map of discrepancy, as well as the simulated values in the observation

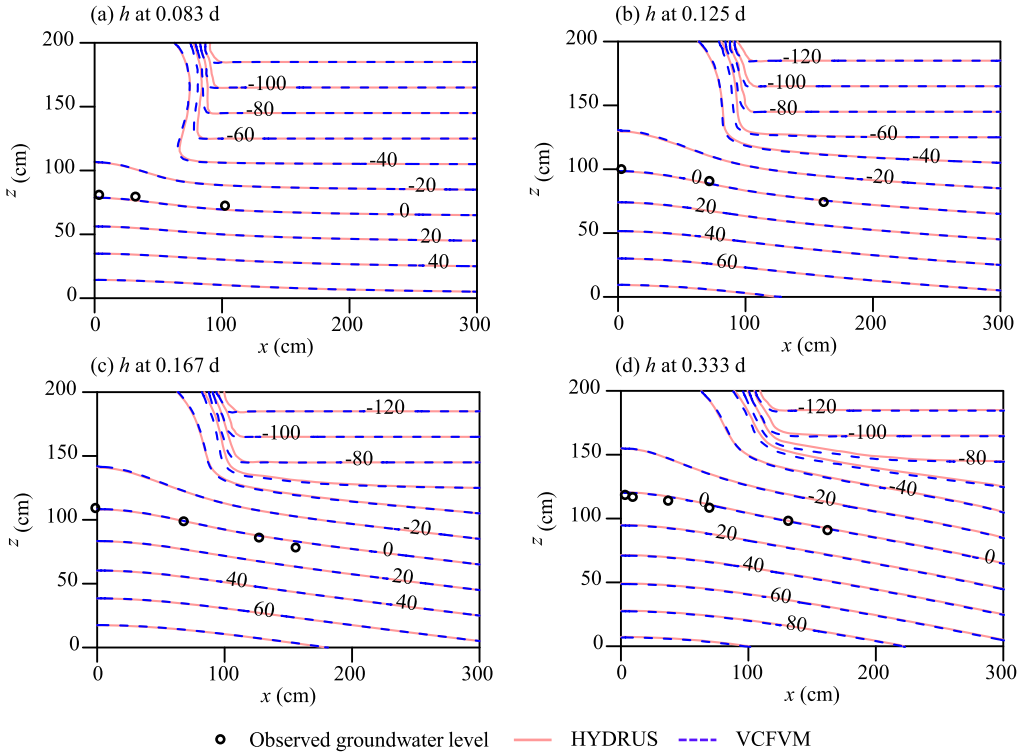


**Fig. 9.** The observed groundwater level and simulated soil water potential obtained by VCFVM and HYDRUS using fine mesh at (a) 0.083 d, (b) 0.125 d, (c) 0.167 d and (d) 0.333 d.

profile ($z = 200$ cm and $0 < x < 100$ cm, as a representative of the locally refined region), are shown in Fig. 10. For a quantitative analysis, we also investigate the MAE and RRMSE of VCFVM with different locally refined meshes by using VCFVM with the fine mesh as benchmark. As for the whole domain, the MAE of VCFVM using M2-a, M2-b and M2-c are 3.51, 2.84 and 2.17 cm, respectively, and the corresponding RRMSE are 6.1%, 5.0% and 4.0%, respectively, which demonstrate the accurate and acceptable results when using locally refined meshes for the whole profile. As for the observation profile, the MAE of VCFVM using M2-a, M2-b and M2-c are 12.00, 7.87 and 0.43 cm, and the corresponding RRMSE values are 35.4%, 23.0% and 1.2%, respectively, which show that the numerical performance of VCFVM becomes better with the increase of the refine level. However, the large errors in M2-a and M2-b for local area (see Fig. 10(g) and (h)) demonstrate that to obtain accurate results for this scenario, the mesh needs to be sufficiently refined at those locations with high hydraulic gradient (such as M2-c).

Furthermore, we discuss the time cost of VCFVM when using different meshes, and the corresponding CPU times are listed in Table 5. It can be found that 1) the CPU time of VCFVM is comparable to that of HYDRUS when using fine mesh; 2) VCFVM is much more efficient when using nonmatching meshes. As the mesh gradually refines, the computational overhead increases. Specifically, the CPU time of VCFVM using M2-c is 53% shorter than that using the fine mesh, and 47% shorter than HYDRUS, which indicates the high efficiency of VCFVM with locally refined meshes. However, as discussed before, the errors of VCFVM using M2-a and M2-b in the observation profile are out of acceptable range (with RRMSE more than 20%), therefore M2-c is recommended for the laboratory experiment case by considering the trade-off between accuracy and efficiency.

### *4.4. Field experiment case: soil water movement under drip irrigation*

The last case is a field experiment with drip irrigation conducted in Hetao Irrigation District, Inner Mongolia, China (108.29°E, 41.17°N). This district has a continental climate with average annual precipitation and evaporation about 170 mm and 2096 mm, respectively. The mainly soil texture is silty loam. The evaporation is about 0.24 cm/d and groundwater depth is about 2.1 m during the experiment. Drip irrigation under film is widely used in this district. The field planting pattern, film and drip tape layout are shown in Fig. 11. The width of the film is 0.6 m, and the drip tape is located in the middle of the film, and the spacing of two drip tapes is 1.0 m, and the spacing of the drippers along the tape is 30 cm. The maize was planted 20 cm away from the tape. During the experiment, the average flux of the dripper is about 777 $cm^3/h$. Three soil profiles were selected as sampling profiles during the experiment, the average value of which were used in the model simulation. Each sampling profile was sampled 3 times (before, during and after drip irrigation), denoted as $T_1 = 0$ d, $T_2 = 0.13$ d and $T_3 = 0.53$ d, respectively. The sampling scheme varies in different sampling times. For $T_1$ and $T_3$, there are five drilling points in horizontal direction for each sampling profile. The drilling points located 0 m (under the dripper), 0.25 m and 0.50 m perpendicular to the drip tape on both sides, and for each drilling point,

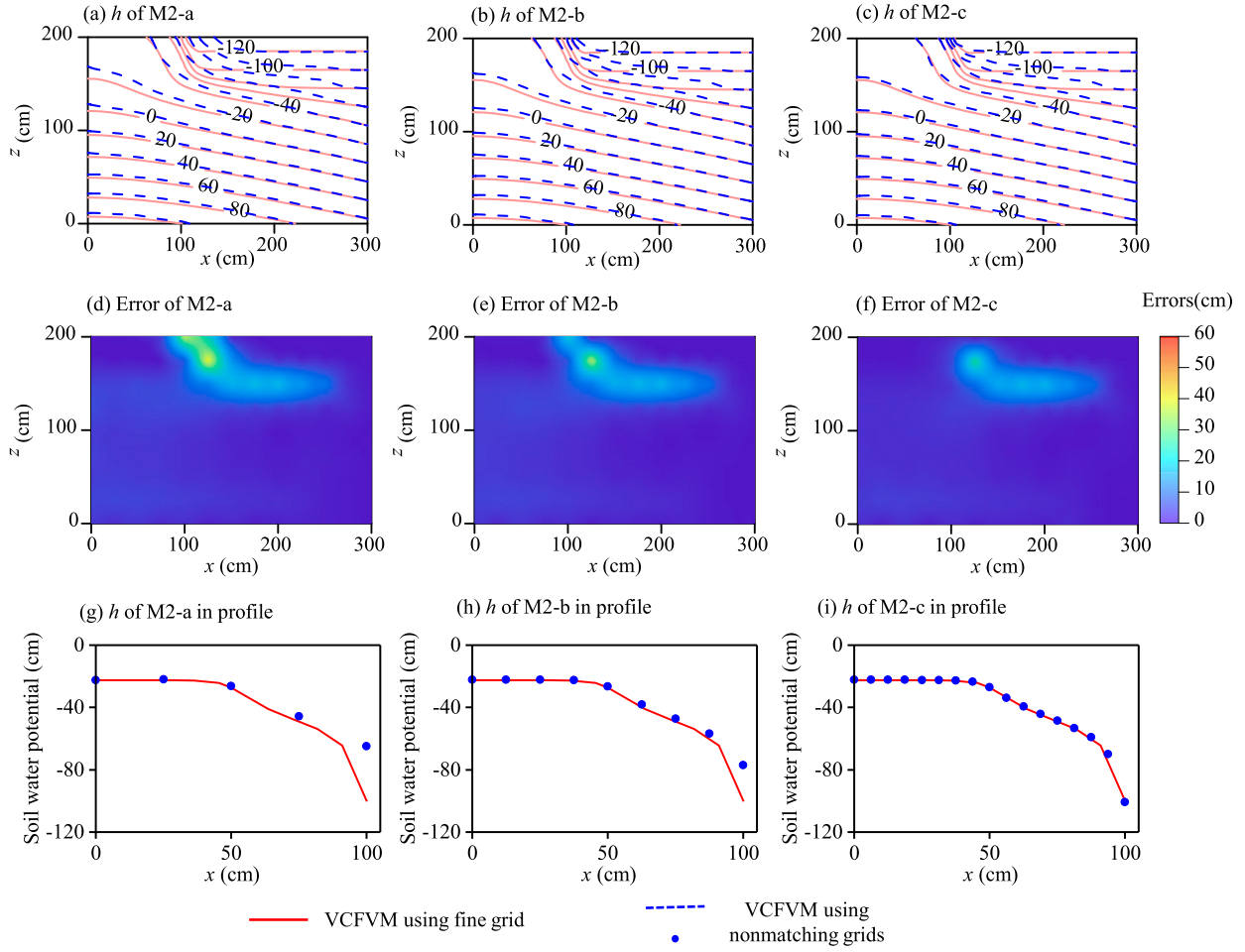


**Fig. 10.** The simulated soil water potentials at 0.333 d of the laboratory experiment case obtained by VCFVM using different grids and the corresponding discrepancy compared with that using fine grid, and the corresponding simulated values in the observation profile.

**Table 8**
The soil hydraulic parameter values of van Genuchten model in the field experiment case.

| Soil depth (cm) | $\theta_r(-)$ | $\theta_s(-)$ | $\alpha(cm^{-1})$ | $n(-)$ | $K_s(cm \cdot d^{-1})$ |
|---|---|---|---|---|---|
| 0-20 | 0.043 | 0.45 | 0.005 | 1.66 | 19.68 |
| 20-40 | 0.068 | 0.45 | 0.005 | 1.66 | 18.72 |
| 40-80 | 0.068 | 0.46 | 0.005 | 1.64 | 22.32 |
| 80-120 | 0.068 | 0.46 | 0.005 | 1.66 | 18.72 |
| 120-210 | 0.069 | 0.46 | 0.005 | 1.66 | 24.00 |

the sample interval along the vertical direction is 10 cm from 0 to 40 cm, while it is 20 cm from 40 to 140 cm. For sampling at $T_2$, there is only one drilling point for each sampling profile, which located under the dripper, and the sample interval along the vertical direction is 10 cm from 0 to 80 cm. The detailed information about the soil sampling scheme at each time level is shown in Fig. 11. The soil particle composition was measured. The averaged sand, silt and clay account for 9.4%, 74.8% and 15.9%, respectively. The observed values at $T_1$ are used as initial values, and observed values at $T_2$ and $T_3$ are used for comparison with the simulated values.

The soil profile with width of 1.0 m and 2.1 m in vertical direction was selected when setting the numerical model, i.e., $\Omega = [0, 100] \times [0, 210]$ cm, shown as the blue section in Fig. 4. The lower boundary was at the groundwater surface. The simulation duration was 0.333 d, and the initial time step was set as $10^{-4}$ d. The soil hydraulic parameters are obtained by calibration using HYDRUS, as given in Table 8, and they are heterogeneous but isotropic in each layer. Since there was no observed value from 1.4 m to 2.1 m, the initial values of this layer were supposed to be linearly change from 0.409 $cm^3/cm^3$ (the observed values at depth of 1.4 m) to 0.46 $cm^3/cm^3$, the saturated soil water content of the layer. The dripper recharge is treated as linear source term along the drip tapes, therefore a point source term in the 2-dimensional cross section perpendicular to the drip tapes. The value of the source term is the ratio of the dipper flux to the spacing of the dipper along the tape. The evaporation and transpiration were not considered

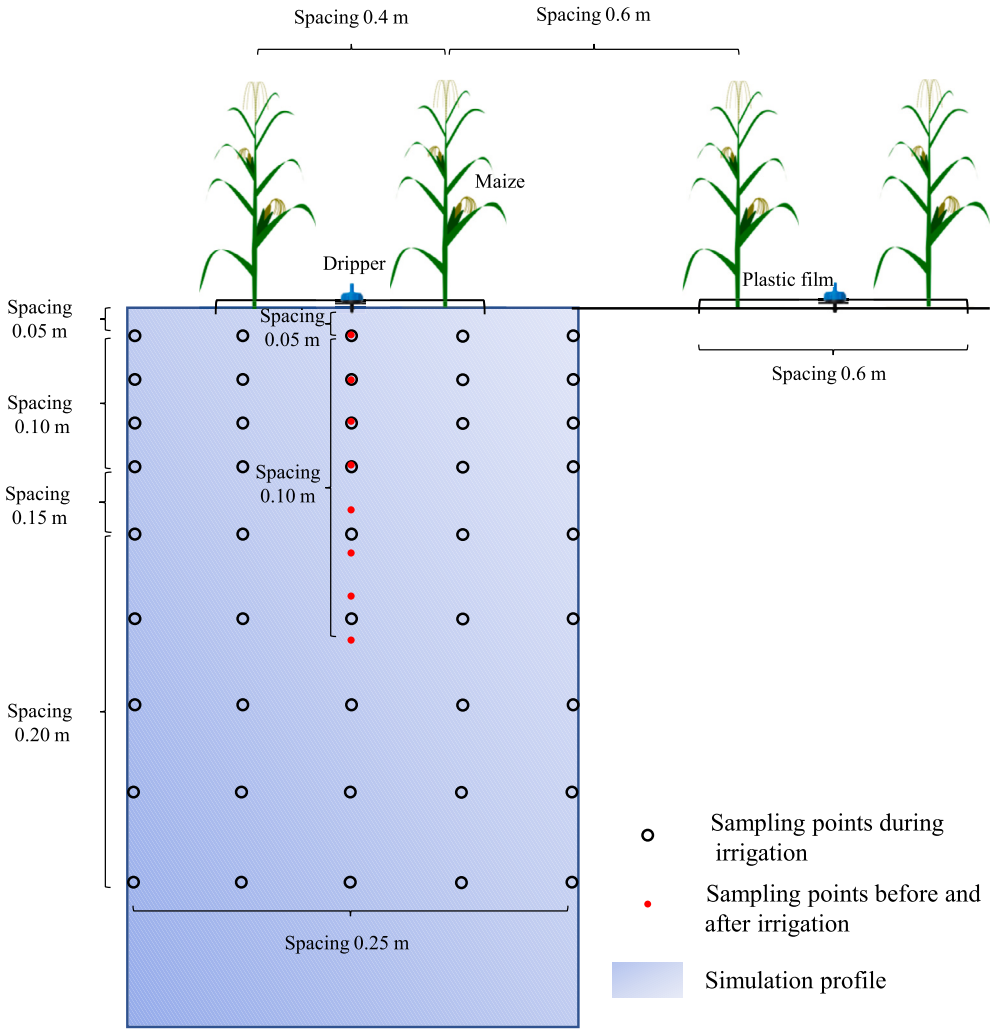


**Fig. 11.** Sketch map of the planting pattern and sampling scheme.

here, since it was negligible compared with the large recharge by dripper. The boundary conditions of this test case are shown in Fig. 2(d), and can be described as follows:

$$h(\boldsymbol{x},t) = 0 \text{ cm}, \ z = 0 \text{ cm},$$

$$K(h)\nabla(h+z)\cdot\boldsymbol{n}(\boldsymbol{x}) = \begin{cases} 0 \text{ cm/d}, & 0 \le x \le 100 \text{ cm}, \ z = 210 \text{ cm}, \\ 0 \text{ cm/d}, & x = 0 \text{ cm}, \ 0 < z \le 210 \text{ cm}, \\ 0 \text{ cm/d}, & x = 100 \text{ cm}, \ 0 < z \le 210 \text{ cm}, \end{cases}$$

$$f(\boldsymbol{x},t) = -621.3 \text{ cm}^2/\text{d}, \ x = 50 \text{ cm}, \ z = 210 \text{ cm}.$$

This case is first simulated by VCFVM using a fine mesh, shown in Fig. 2(d), and the simulated results at $T_2$ and $T_3$ are compared with the corresponding observed values, as well as the results simulated by HYDRUS using the same mesh. Then the case is simulated by VCFVM using different locally refined meshes to show its superiority. Since the hydraulic gradient is high near the dripper, this location is selected for local refinement, and three nonmatching meshes locally refined with quadrilateral elements, denoted as M3-a, M3-c, and M3-d, as well as a mesh locally refined with triangular elements, denoted as M3-b, are used here for simulation, as shown in Fig. 12. The basic information of the fine mesh and three locally refined meshes used in the field experiment case is given in Table 3.

The simulated soil water content in the soil profiles at different distances to the dripper and different time stamps obtained by VCFVM and HYDRUS using the same fine mesh, as well as the observed values are shown in Fig. 13. Compared to the observed values, the MAE of VCFVM in soil profiles under dripper at $T_2 = 0.13$ d, as well as 0.5 m, 0.25 m and 0 m to dripper at $T_3 = 0.53$ d are

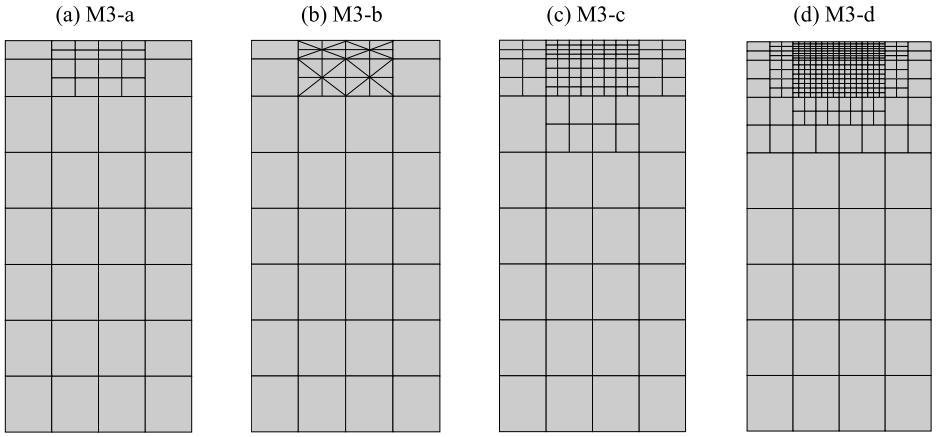


**Fig. 12.** Locally refined meshes used in the field experiment case.

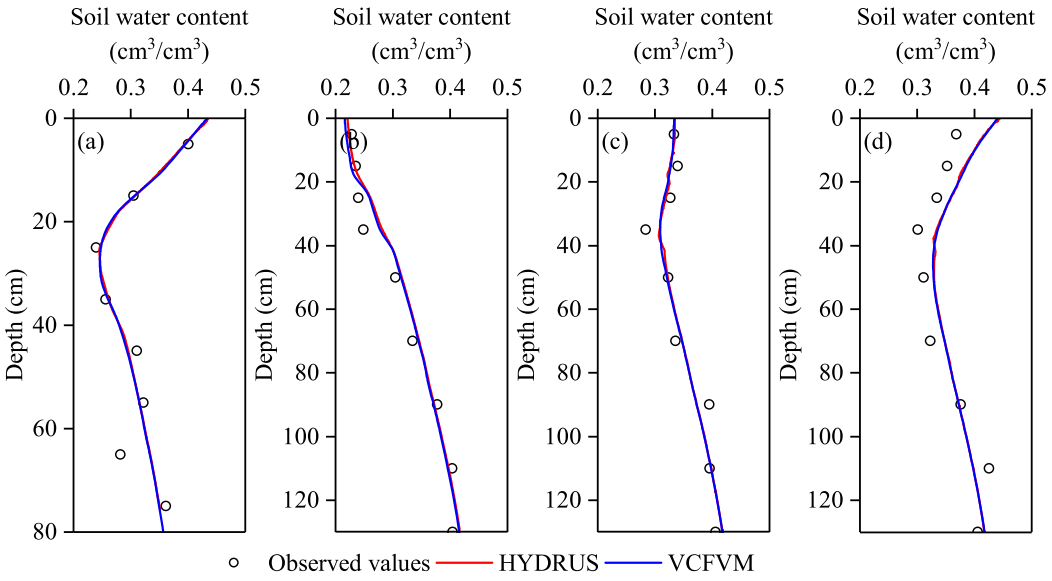


**Fig. 13.** The observed and simulated soil water contents ($\theta$) obtained by VCFVM and HYDRUS using the same fine mesh in the field experiment case with the soil profile: (a) under dripper at 0.13 d, (b) 0.5 m to dripper at 0.53 d, (c) 0.25 m to dripper at 0.53 d and (d) 0 m to dripper at 0.53 d.

0.015, 0.012, 0.011 and 0.026 $cm^3/cm^3$, respectively, and the corresponding RRMSE are 6.8%, 4.8%, 4.0% and 8.3%. For HYDRUS, the MAE in soil profiles under dripper at $T_2 = 0.13$ d, as well as 0.5 m, 0.25 m and 0 m to dripper at $T_3 = 0.53$ d are 0.013, 0.012, 0.011 and 0.025 $cm^3/cm^3$, respectively, and the corresponding RRMSE are 6.4%, 4.9%, 3.8% and 7.9%. The consistent MAE and RRMSE between VCFVM and HYDRUS indicate the consistent accuracy of them.

To make it clearer, contour maps of the simulated soil water contents ($\theta$) and water potential ($h$) in the whole domain at $T_2 = 0.13$ d and $T_3 = 0.53$ d obtained by VCFVM and HYDRUS, and the corresponding discrepancies between them are shown in Fig. 14. It can be found that the results simulated by VCFVM match well with those by HYDRUS. Compared to HYDRUS, the MAE of soil water contents simulated by VCFVM are 0.0006 $cm^3/cm^3$ and 0.0006 $cm^3/cm^3$ at $T_2 = 0.13$ and $T_3 = 0.53$ d, respectively, and the corresponding RRMSE are 0.2% and 0.1%, and the MAE of soil water potentials obtained by VCFVM are 1.904 cm and 1.433 cm, and the corresponding RRMSE are 0.7% and 0.8%. Once again, the results show that the accuracy of VCFVM is consistent with that of HYDRUS in practical scenarios with heterogeneous soil using the uniform fine triangular meshes.

To evaluate the accuracy of VCFVM with locally refined meshes in this case, the simulated soil water contents ($\theta$) in the observation profiles ($x = 0$ cm, 25 cm and 50 cm) at $T_3 = 0.53$ d obtained by VCFVM using different locally refined meshes (denoted as M3-a, M3-b, M3-c and M3-d) compared to the corresponding observed values are shown in Fig. 15. The RRMSE values of the four locally refined meshes range from 4.1% to 4.6%. Both Fig. 15 and the RRMSE values demonstrate the consistent accuracy among the different meshes compared to the observed values.

In order to avoid the influence of the limited number of observed values, the simulated values using those locally refined meshes are also compared to the results obtained using the fine mesh. The simulated soil water contents ($\theta$) in the whole domain at

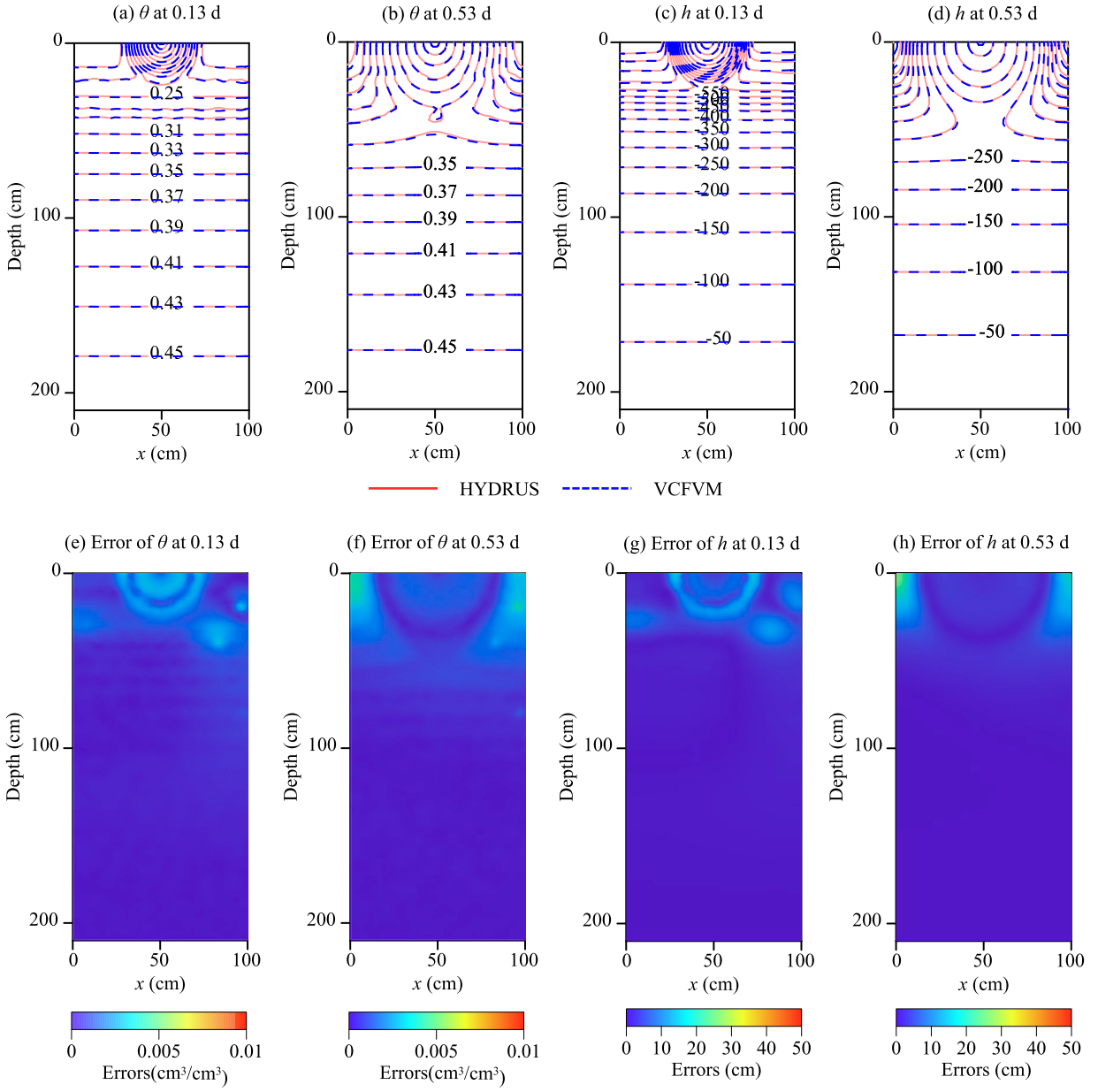


**Fig. 14.** The simulated soil water contents ($\theta$) and potentials ($h$) at 0.13 d and 0.53 d obtained by VCFVM and HYDRUS using the same fine mesh, and the corresponding discrepancies between the results generated by them.

$T_3 = 0.53$ d obtained by VCFVM using different locally refined meshes compared with that using the fine mesh, and the corresponding discrepancy, as well as the corresponding simulated values in the observation profiles comparing with observations, are shown in Fig. 16. It can be found that all MAE values of the four locally refined meshes are lower than 0.011 $cm^3/cm^3$ for the observation profiles, and lower than 0.006 $cm^3/cm^3$ for the whole domain. Even for the grids used as M3-a with 61 vertices, the simulation accuracy was still acceptable. When the vertices number comes to 138 as shown in M3-c, the MAE value for the whole domain reduces to 0.003 $cm^3/cm^3$ compared to the results using the fine mesh with 1106 vertices. It further reduces to 0.002 $cm^3/cm^3$ when using M3-d with 391 vertices. Moreover, the consistent MAE values of M3-a and M3-b demonstrate the applicability of VCFVM to different kinds of meshes. It can be concluded that VCFVM could simulate soil water flow using locally refined meshes, and the accuracy increase with the increase of the vertices.

In regards to the efficiency of VCFVM with locally refined meshes in this case, as listed in Table 5, the CPU time increases with the increase of the number of vertices as expected, and the CPU times are still 45% shorter than that using the fine mesh when use M3-d, and 36% shorter than HYDRUS, which indicates the high efficiency of VCFVM with locally refined mesh. However, different with the laboratory experiment case, in this case, all of the RRMSE of locally refined meshes are quite low and within acceptable

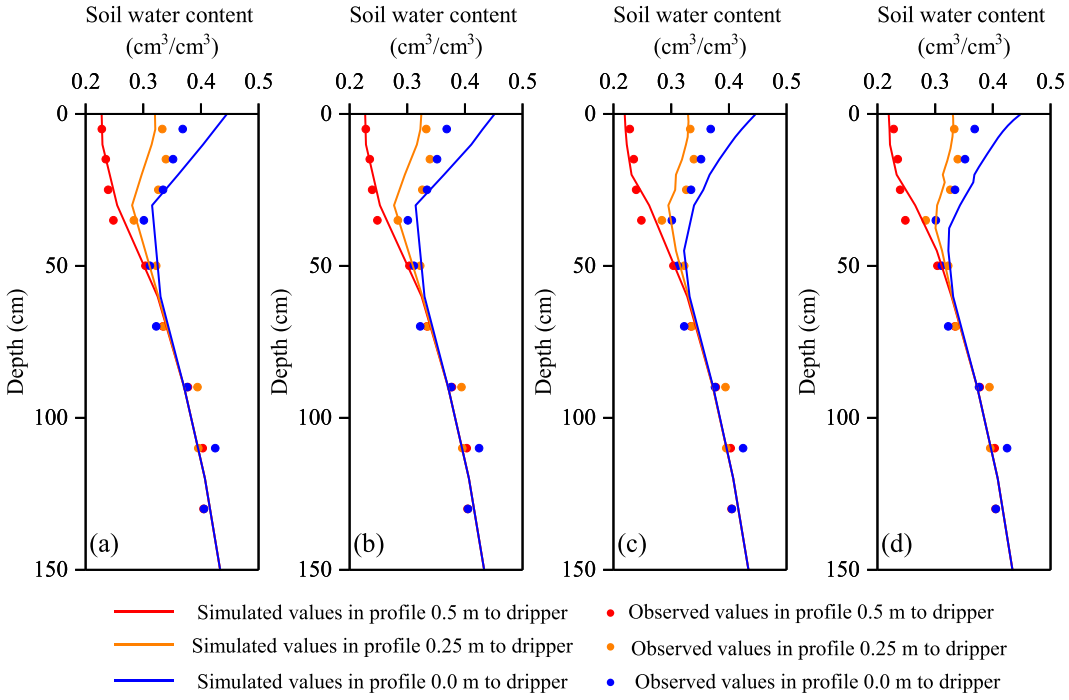


**Fig. 15.** The simulated soil water contents in the observation profiles at 0.53 d obtained by VCFVM in the field experiment case using different locally refined meshes: M3-a, M3-b, M3-c and M3-d (from left to right), compared to the corresponding observed values.

range (lower than 4%), therefore M3-a is recommended for this case in order to increase the efficiency without sacrificing much accuracy.

## 5. Conclusions

A numerical algorithm based on vertex-centered finite volume method is developed to solve Richards' Equation with locally refined meshes. The algorithm was tested by several cases with different soil types and boundary conditions. Our study leads to the following major conclusions: a) VCFVM can obtain accurate results of soil water potential and soil water content when involving wide range of soil types and different boundary conditions, as well as those practical simulation; b) The VCFVM can deal with soil water flow by using different kinds of locally refined meshes, especially nonmatching meshes, with high accuracy and efficiency; c) The refined grids are recommended to cover those regions with high nonlinear soil water potential change. Our work is expected to provide an effective numerical method with ability to solve Richards' Equation via nonmatching grids, which is appealing in those scenarios involving source/sink terms or boundary conditions with scales much smaller than the simulation domain, but with dramatic head gradients, such as drip irrigation, subsurface drainage pipes, open ditches, and so on. Furthermore, the soil solute transport numerical models with higher efficiency also could be developed based on the proposed VCFVM scheme.

## CRediT authorship contribution statement

**Yingzhi Qian:** Methodology, Writing – original draft. **Xiaoping Zhang:** Methodology, Writing – review & editing, Writing – original draft. **Yan Zhu:** Methodology, Writing – review & editing. **Lili Ju:** Methodology, Writing – review & editing. **Alberto Guadagnini:** Writing – review & editing. **Jiesheng Huang:** Writing – review & editing.

## Declaration of competing interest

The authors declare that they have no known competing financial interests or personal relationships that could have appeared to influence the work reported in this paper.

## Data availability

Data will be made available on request.

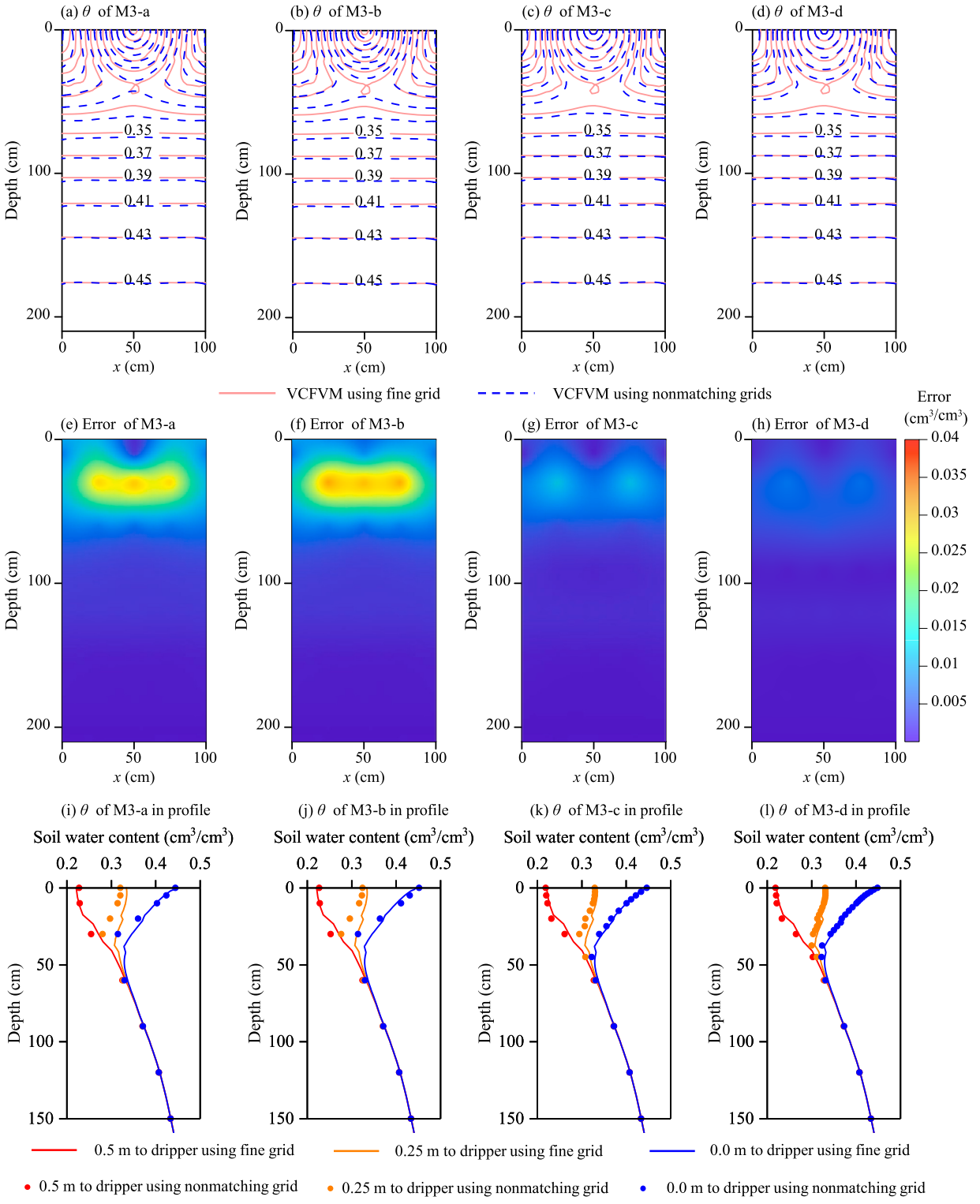


**Fig. 16.** The simulated soil water contents at 0.53 d of Case 3 obtained by VCFVM using different grids and the corresponding discrepancy compared with that using fine grids, and the corresponding simulated values in the observation profiles.

## Acknowledgements

Y. Zhu's research is partially supported by Natural Science Foundation of China (52179041), National Key Research and Development Program of China (2021YFD1900805-02). Y. Qian's research is partially supported by the China Scholarship Council (202106270106). L. Ju's research is partially supported by U.S. National Science Foundation (DMS-2109633).

## References

[1] J. Arnold, D. Moriasi, P. Gassman, K. Abbaspour, M. White, R. Srinivasan, C. Santhi, R. Harmel, A. van Griensven, M. Van Liew, N. Kannan, M. Jha, Swat: model use, calibration, and validation, Trans. ASABE 55 (2012) 1491–1508, https://doi.org/10.13031/2013.42256.
[2] R.F. Carsel, R.S. Parrish, Developing joint probability distributions of soil-water retention characteristics, Water Resour. Res. 24 (1988) 755–769, https://doi.org/10.1029/WR024i005p00755.
[3] M. Celia, E. Bouloutas, R. Zarba, A general mass-conservative numerical solution for the unsaturated flow equation, Water Resour. Res. 26 (1990) 1483–1496, https://doi.org/10.1029/WR026i007p01483.
[4] J. Clément, F. Golay, M. Ersoy, D. Sous, An adaptive strategy for discontinuous Galerkin simulations of Richards' equation: application to multi-materials dam wetting, Adv. Water Resour. 3 (2021) 103897, https://doi.org/10.1016/j.advwatres.2021.103897.
[5] Q. Dong, J. Wu, S. Su, Relationship between the vertex-centered linearity-preserving scheme and the lowest-order virtual element method for diffusion problems on star-shaped polygon, Comput. Math. Appl. 79 (2020) 3117–3138, https://doi.org/10.1016/j.camwa.2020.01.009.
[6] M. Farthing, F. Ogden, Numerical solution of Richards' equation: a review of advances and challenges, Soil Sci. Soc. Am. J. 81 (2017) 1257–1269, https://doi.org/10.2136/sssaj2017.02.0058.
[7] G. Feng, C. Zhu, Q. Wu, C. Wang, Z. Zhang, R.M. Mwiya, L. Zhang, Evaluating the impacts of saline water irrigation on soil water-salt and summer maize yield in subsurface drainage condition using coupled hydrus and epic model, Agric. Water Manag. 258 (2021) 107175, https://doi.org/10.1016/j.agwat.2021.107175.
[8] Y. Gao, Y. Li, A mortar mixed finite volume method for elliptic problems on nonmatching multi-block triangular grids, J. Sci. Comput. 72 (2017) 50–69, https://doi.org/10.1007/s10915-017-0405-z.
[9] M. van Genuchten, A closed-form equation for predicting the hydraulic conductivity of unsaturated soils, Soil Sci. Soc. Am. J. 44 (1980) 892–898, https://doi.org/10.2136/sssaj1980.03615995004400050002x.
[10] T. Hou, X. Wu, A multiscale finite element method for elliptic problems in composite materials and porous media, J. Comput. Phys. 134 (1997) 169–189, https://doi.org/10.1006/jcph.1997.5682.
[11] R. Huber, R. Helmig, Multiphase flow in heterogeneous porous media: a classical finite element method versus an implicit pressure-explicit saturation-based mixed finite element-finite volume approach, Int. J. Numer. Methods Fluids 29 (1999) 899–920, https://doi.org/10.1002/(SICI)1097-0363(19990430)29:8<899::AID-FLD715>3.0.CO;2-W.
[12] A.R. Isa-Abadi, V. Fontaine, H.R. Ghafouri, A. Younes, M. Fahs, A fully interior penalty discontinuous Galerkin method for variable density groundwater flow problems, Comput. Fluids 213 (2020) 104744, https://doi.org/10.1016/j.compfluid.2020.104744.
[13] J. Kroes, J. van Dam, R. Bartholomeus, P. Groenendijk, M. Heinen, I. Supit, P. van Walsum, A mortar mixed finite volume method for elliptic problems on nonmatching multi-block triangular grids, J. Sci. Comput. 72 (2017) 50–69, https://doi.org/10.1007/s10915-017-0405-z.
[14] C. Langevin, J. Hughes, E. Banta, R. Niswonger, S. Panday, A. Provost, A fully interior penalty discontinuous Galerkin method for variable density groundwater flow problems, Comput. Fluids 213 (2017) 104744, https://doi.org/10.1016/j.compfluid.2020.104744.
[15] F. Lehmann, P. Ackerer, Comparison of iterative methods for improved solutions of the fluid flow equation in partially saturated porous media, Transp. Porous Media 31 (1998) 275–292, https://doi.org/10.1023/a:1006555107450.
[16] E. Lekakis, V. Antonopoulos, Modeling the effects of different irrigation water salinity on soil water movement, uptake and multicomponent solute transport, J. Hydrol. 530 (2015) 431–446, https://doi.org/10.1016/j.jhydrol.2015.09.070.
[17] H. Li, M.W. Farthing, C.N. Dawson, C.T. Miller, Local discontinuous Galerkin approximations to Richards' equation, Adv. Water Resour. 30 (2007) 555–575, https://doi.org/10.1016/j.advwatres.2006.04.011.
[18] F. List, F. Radu, A study on iterative methods for solving Richards' equation, Comput. Geosci. 20 (2016) 341–353, https://doi.org/10.1007/s10596-016-9566-3.
[19] I. Lunati, M. Tyagi, S. Lee, An iterative multiscale finite volume algorithm converging to the exact solution, J. Comput. Phys. 230 (2011) 1849–1864, https://doi.org/10.1016/j.jcp.2010.11.036.
[20] W. Mao, J. Yang, Y. Zhu, M. Ye, Z. Liu, J. Wu, An efficient soil water balance model based on hybrid numerical and statistical method, J. Hydrol. 559 (2018) 721–735, https://doi.org/10.1016/j.jhydrol.2018.02.074.
[21] W. Mao, Y. Zhu, J. Wu, M. Ye, J. Yang, Modelling the salt accumulation and leaching processes in arid agricultural areas with a new mass balance model, J. Hydrol. 591 (2020) 125329, https://doi.org/10.1016/j.jhydrol.2020.125329.
[22] S. Mehl, M. Hill, Development and evaluation of a local grid refinement method for block-centered finite-difference groundwater models using shared nodes, Adv. Water Resour. 25 (2002) 497–511, https://doi.org/10.1016/S0309-1708(02)00021-0.
[23] C.T. Miller, C. Abhishek, M.W. Farthing, A spatially and temporally adaptive solution of Richards' equation, Adv. Water Resour. 29 (2006) 525–545, https://doi.org/10.1016/j.advwatres.2005.06.008.
[24] C.T. Miller, C. Abhishek, A.B. Sallerson, J.F. Prins, M.W. Farthing, A comparison of computational and algorithmic advances for solving Richards' equation, Dev. Water Sci. 2 (2004) 1131–1145, https://doi.org/10.1016/S0167-5648(04)80130-8.
[25] R. Mose, P. Siegel, P. Ackerer, Application of the mixed hybrid finite element approximation in a groundwater flow model: luxury or necessity?, Water Resour. Res. 30 (1994) 3001–3012, https://doi.org/10.1029/94WR01786.
[26] R. Oosterbaan, Saltmod: description of principles and applications, Water Resour. Res. 30 (1998) 3001–3012, https://doi.org/10.1029/94WR01786.
[27] L. Orgogozo, N. Renon, C. Soulaine, F. Henon, S. Tomer, D. Labat, O. Pokrovsky, M. Sekhar, R. Ababou, M. Quintard, An open source massively parallel solver for Richards equation: mechanistic modelling of water fluxes at the watershed scale, Comput. Phys. Commun. 185 (2014) 3358–3371, https://doi.org/10.1016/j.cpc.2014.08.004.
[28] C. Paniconi, M. Putti, A comparison of Picard and Newton iteration in the numerical solution of multidimensional variably saturated flow problems, Water Resour. Res. 30 (1994) 3357–3374, https://doi.org/10.1029/94WR02046.
[29] Y. Qian, Y. Zhu, X. Zhang, J. Wu, M. Ye, W. Mao, J. Wu, J. Huang, J. Yang, A local grid-refined numerical groundwater model based on the vertex-centred finite-volume method, Adv. Water Resour. 173 (2023) 104392.
[30] K. Ranatunga, E. Nation, D. Barratt, Review of soil water models and their applications in Australia, Environ. Model. Softw. 23 (2008) 1182–1206, https://doi.org/10.1016/j.envsoft.2008.02.003.
[31] L. Richards, Capillary conduction of liquids through porous medium, Physics 1 (1931) 318–333, https://doi.org/10.1063/1.1745010.
[32] D.M. Romero, S.E. Silver, Grid cell distortion and modflow's integrated finite difference numerical solution, Groundwater 44 (2006) 797–802, https://doi.org/10.1111/j.1745-6584.2005.00179.x.
[33] J. Shewchuk, What is a good linear finite element-interpolation, conditioning, anisotropy, and quality measures, in: Proceedings of the 11th International Meshing Roundtable 44, 2006, pp. 797–802.

[34] J. Simunek, M. van Genuchten, M. Sejna, The hydrus software package for simulating the two- and three-dimensional movement of water, heat, and multiple solutes in variably-saturated media, in: Proceedings of the 11th International Meshing Roundtable 44, 2006, pp. 797–802.
[35] J. Simunek, M. van Genuchten, M. Sejna, Recent developments and applications of the hydrus computer software packages, Vadose Zone J. 15 (2016) 1–25, https://doi.org/10.2136/vzj2016.04.0033.
[36] S. Su, Q. Dong, J. Wu, A vertex-centered and positivity-preserving scheme for anisotropic diffusion equations on general polyhedral meshes, Math. Methods Appl. Sci. 42 (2019) 59–84.
[37] R. Thomas, R. Johnson, R. Healy, User's guide to the variably saturated flow (vsf) process for modflow, Techniques and Methods 6-A18 15, 2016, pp. 1–25, http://pubs.usgs.gov/tm/2006/tm6a18.
[38] N. Twarakavi, J. Simunek, S. Seo, Evaluating interactions between groundwater and vadose zone using the hydrus-based flow package for modflow, Vadose Zone J. 7 (2016) 1–25, https://doi.org/10.2136/vzj2009.0190.
[39] M. Vauclin, J. Khanji, G. Vachaud, Experimental and numerical study of a transient, two-dimensional unsaturated–saturated water table recharge problem, Water Resour. Res. 15 (1979) 1089–1101, https://doi.org/10.1029/wr015i005p01089.
[40] J. Wu, Vertex-centered linearity-preserving schemes for nonlinear parabolic problems on polygonal grids, J. Sci. Comput. 71 (2017) 499–524, https://doi.org/10.1007/s10915-016-0309-3.
[41] J. Wu, Z. Gao, Z. Dai, A vertex-centered linearity-preserving discretization of diffusion problems on polygonal meshes, J. Comput. Phys. 81 (2016) 131–150, https://doi.org/10.1002/fld.4178.
[42] Y. Xie, C. Lu, Y. Xue, Y. Ye, C. Xie, H. Ji, J. Wu, New finite volume multiscale finite element model for simultaneously solving groundwater flow and Darcian velocity fields in porous media, J. Hydrol. 15 (2016) 592–606, https://doi.org/10.1016/j.jhydrol.2019.04.004.
[43] Y. Zha, L. Shi, Y. Ming, J. Yang, A generalized Ross method for two- and three-dimensional variably saturated flow, Adv. Water Resour. 54 (2013) 67–77, https://doi.org/10.1016/j.advwatres.2013.01.002.
[44] Y. Zha, J. Yang, J. Zeng, M. Tso, W. Zeng, L. Shi, Review of numerical solution of Richardson-Richards equation for variably saturated flow in soils, Water 6 (2019) e1364, https://doi.org/10.1002/wat2.1364.
[45] X. Zhang, S. Su, J. Wu, A vertex-centered and positivity-preserving scheme for anisotropic diffusion problems on arbitrary polygonal grids, J. Comput. Phys. 344 (2017) 419–436, https://doi.org/10.1016/j.jcp.2017.04.070.